Orographic Flow Influence on Precipitation During an Atmospheric River Event at Davis, Antarctica

Josué Gehring, Étienne Vignon, Anne-claire Billault-roux, Alfonso Ferrone, Alain Protat, Simon P Alexander, Alexis Berne

JGR Atmospheres

RESEARCH ARTICLE
10.1029/2021JD035210

Special Section:
Southern Ocean clouds, aerosols, precipitation and radiation

Orographic Flow Influence on Precipitation During an Atmospheric River Event at Davis, Antarctica

Josué Gehring[1], Étienne Vignon[2,1], Anne-Claire Billault-Roux[1], Alfonso Ferrone[1], Alain Protat[3,4], Simon P. Alexander[5,4], and Alexis Berne[1]

[1]Environmental Remote Sensing Laboratory (LTE), École Polytechnique Fédérale de Lausanne (EPFL), Lausanne, Switzerland, [2]Laboratoire de Météorologie Dynamique/IPSL/Sorbone Université/CNRS, UMR, Paris, France, [3]Bureau of Meteorology, Melbourne, VIC, Australia, [4]Australian Antarctic Program Partnership, Institute for Marine and Antarctic Science, University of Tasmania, Hobart, TAS, Australia, [5]Australian Antarctic Division, Kingston, TAS, Australia

Abstract Intense snowfall sublimation was observed during a precipitation event over Davis in the Vestfold Hills, East Antarctica, from 08 to 10 January 2019. Radar observations and simulations from the Weather Research and Forecasting model revealed that orographic gravity waves (OGWs), generated by a north-easterly flow impinging on the ice ridge upstream of Davis, were responsible for snowfall sublimation through a foehn effect. Despite the strong meridional moisture advection associated with an atmospheric river (AR) during this event, almost no precipitation reached the ground at Davis. We found that the direction of the synoptic flow with respect to the orography determined the intensity of OGWs over Davis, which in turn directly influenced the snowfall microphysics. We hypothesize that turbulence induced by the OGWs likely enhanced the aggregation process, as identified thanks to dual-polarization and dual-frequency radar observations. This study suggests that despite the intense AR, the precipitation distribution was determined by local processes tied to the orography. The mechanisms found in this case study could contribute to the extremely dry climate of the Vestfold Hills, one of the main Antarctic oases.

Plain Language Summary A case study of a snowfall event over Davis, Antarctica is presented. Despite the strong precipitation, snowfall did not reach the ground due to intense sublimation (transition from solid to gas state). Meteorological radar observations and atmospheric model simulations revealed that a dry downslope wind was responsible for the sublimation of snowfall below the cloud base. Despite the intense transport of moisture associated with the low pressure system during this event, almost no precipitation reached the ground at Davis. We found that the wind direction with respect to the main ridge upstream of Davis determined the intensity of the sublimation. This study suggests that despite favorable large-scale conditions for intense snowfall at Davis, local processes related to the topography determined how much precipitation reached the ground. The mechanisms found in this case study could contribute to the extremely dry climate of the Vestfold Hills, one of the main ice-free regions of Antarctica.

Key Points:

- Despite intense moisture advection by an atmospheric river, foehn winds tied to orographic gravity waves (OGWs) led to snowfall sublimation
- The flow direction determined the intensity of the foehn and hence the temporal and spatial precipitation variability
- The event can be divided into three phases during which the features of the OGWs influenced the observed microphysics in distinct ways

Correspondence to:
A. Berne,
alexis.berne@epfl.ch

Citation:
Gehring, J., Vignon, É., Billault-Roux, A.-C., Ferrone, A., Protat, A., Alexander, S. P., & Berne, A. (2022). Orographic flow influence on precipitation during an atmospheric river event at Davis, Antarctica. *Journal of Geophysical Research: Atmospheres*, *127*, e2021JD035210. https://doi.org/10.1029/2021JD035210

Received 7 MAY 2021
Accepted 14 DEC 2021

Author Contributions:
Conceptualization: Josué Gehring, Étienne Vignon, Alexis Berne
Data curation: Josué Gehring, Étienne Vignon, Anne-Claire Billault-Roux, Alfonso Ferrone, Alain Protat, Simon P. Alexander
Formal analysis: Josué Gehring, Étienne Vignon, Anne-Claire Billault-Roux, Alfonso Ferrone, Alain Protat, Simon P. Alexander, Alexis Berne
Funding acquisition: Alexis Berne

1. Introduction

Snowfall in Antarctica is the main input to ice sheet mass balance (King & Turner, 1997), which determines the contribution of the southernmost continent to sea level rise (Shepherd & Wingham, 2007). On the East Antarctic coast, most of the precipitation comes either from meridional moisture advection by extratropical cyclones or is induced by orographic forcing (King & Turner, 1997). The surface mass balance of the East Antarctic coastal ice sheets is hence heavily influenced by the frequency and intensity of maritime moisture intrusions from lower latitudes, which often result in high precipitation accumulations (Noone et al., 1999; Nuncio & Satheesan, 2014; Welker et al., 2014). A recent study by Turner et al. (2019) showed that extreme precipitation events (EPEs, defined as the largest 10% of daily totals) contribute to more than 40% of the annual precipitation over much of the continent. In particular, the greatest contribution from EPEs is found on the main ice shelves, especially on the Amery Ice Shelf (less than 10 days of the highest-ranked precipitation contributing to 50% of the annual total). Davis station (69°S, 78°E) is located on the coast of the Vestfold Hills, just north-east of the Amery Ice Shelf (Figure 1). The Vestfold Hills are one of the few ice-free regions in Antarctica, which makes it part of the Antarctic oases (Pickard, 1986). This is due mostly to its precipitation climatology with only 70.9 mm mean annual precipitation and 7.5 mm in December–January–February (DJF, statistics computed over the period 1960–2021, http://www.bom.gov.au/climate/averages/tables/cw_300000_All.shtml). Davis station, with its 1.8 ° C mean daily

Investigation: Josué Gehring, Simon P. Alexander
Methodology: Josué Gehring
Project Administration: Simon P. Alexander, Alexis Berne
Resources: Alexis Berne
Supervision: Alexis Berne
Visualization: Josué Gehring, Étienne Vignon, Anne-Claire Billault-Roux, Alfonso Ferrone
Writing – original draft: Josué Gehring
Writing – review & editing: Josué Gehring, Étienne Vignon, Anne-Claire Billault-Roux, Alfonso Ferrone, Alain Protat, Simon P. Alexander, Alexis Berne

maximum temperature and 8.3 h mean daily sunshine in DJF, is known as the "Antarctic Riviera" (Summerson & Bishop, 2011), because it is both relatively warm and dry. According to Turner et al. (2019), EPEs contribute to about 55% of the annual total precipitation in the Vestfold Hills with more than 95% of the interannual variability explained by EPEs. This shows that in the dry climate of Davis, EPEs have a significant climatological impact. In Antarctica, EPEs are often associated with narrow corridors of enhanced integrated water vapor (IWV) and integrated vapor transport, called atmospheric rivers (ARs, Ralph et al., 2004; Zhu & Newell, 1998). Indeed, Gorodetskaya et al. (2014) showed that ARs were responsible for outstanding precipitation accumulations over coastal Dronning Maud land, East Antarctica. Moreover, Wille et al. (2021) concluded that ARs are responsible for at least 10% of accumulated snowfall over East Antarctica and a majority of EPEs. However, the fate of these intense meridional moisture advection events depends on the state of the coastal boundary layer. For instance, Grazioli et al. (2017) showed that snowfall sublimation by dry katabatic winds leads to a decrease of 17% of total snowfall on the continental scale and up to 35% on the margins of East Antarctica, consistent with the more recent study of Agosta et al. (2019). While, this low-level sublimation is very effective for light snowfall events, Grazioli et al. (2017) showed that it can still lead to a decrease of about 20% for the most intense snowfall cases over Dumont d'Urville, East Antarctica. This shows that katabatic winds can substantially affect the total amount at ground level during EPEs. However, other atmospheric processes might contribute to low-level snowfall sublimation. For instance, foehn winds, which are common in the Antarctic Peninsula (Elvidge et al., 2015; Grosvenor et al., 2014; Kirchgaessner et al., 2021) and in the McMurdo Dry Valleys (Speirs et al., 2010; Steinhoff et al., 2013), can lead to record-setting warming and drying of the air in the lee of a mountain (Bozkurt et al., 2018). While, the impact of foehn on melting and sublimation of ice shelves has been already studied (Cape et al., 2015; Zou et al., 2019), its effect on snowfall sublimation in Antarctica has, to our knowledge, never been investigated. Foehn winds are associated with orographic gravity waves (OGWs) (Damiens et al., 2018; Elvidge et al., 2016; Vosper et al., 2018), which, in East Antarctica, are generated when synoptic or katabatic winds impinge upon a mountain ridge or reach the coast (Valkonen et al., 2010; Watanabe et al., 2006) and they can be trapped downstream of a katabatic jump (Vignon et al., 2020). Alexander et al. (2017) studied a gravity wave event at Davis and found that the gravity waves were generated by the interaction between a strong north-easterly synoptic flow and the orography upstream of Davis. These OGWs were responsible for temperature fluctuations that affect the formation of cirrus clouds. While, OGWs in East Antarctica have been the subject of investigations in the last two decades (Alexander & Murphy, 2015; Moffat-Griffin, 2019; Orr et al., 2014; Watanabe et al., 2006), their impact on precipitation remains to be determined.

The goal of this study is to investigate how the synoptic evolution of an intense precipitation event (08–10 January 2019) and the local orography influenced the precipitation distribution and microphysics over the Vestfold Hills. We use recent data collected during the Precipitation over Land And The Southern Ocean (PLATO) campaign at Davis. This includes scanning polarimetric and vertically pointing Doppler radar measurements at different frequencies, as well as radiosounding data and a Raman lidar. We also make use of simulations from the Weather Research and Forecasting (WRF) model. We address the following questions:

1. How does the synoptic flow constrain the presence of OGWs?
2. How do foehn winds impact snowfall sublimation and the spatial distribution of precipitation during this event?
3. How do OGWs influence the snowfall microphysical evolution?

This paper is structured as follows. Section 2 describes the geography of Davis and the data set. Section 3 presents the evolution of the synoptic conditions and the precipitation distribution of this case study. In Section 4 we analyze the dynamics and microphysics of the event during three distinct phases. The possible climatological relevance of this case study is discussed in Section 5. We finally summarize and conclude this paper in Section 6.

2. Vestfold Hills Geography and the PLATO Campaign at Davis

PLATO is a project coordinated and logistically supported by the Australian Antarctic Division that aims to characterize precipitation over the Southern Ocean and Antarctica, and evaluate the precipitation products obtained by satellites and atmospheric models. The central field campaign was organized at Davis with an intensive observation period from November 2018 to February 2019. Davis is located in the Vestfold Hills, one of the few ice-free regions of Antarctica, at the foot of a steep transition from the elevated ice sheet to the coast (Figure 1).

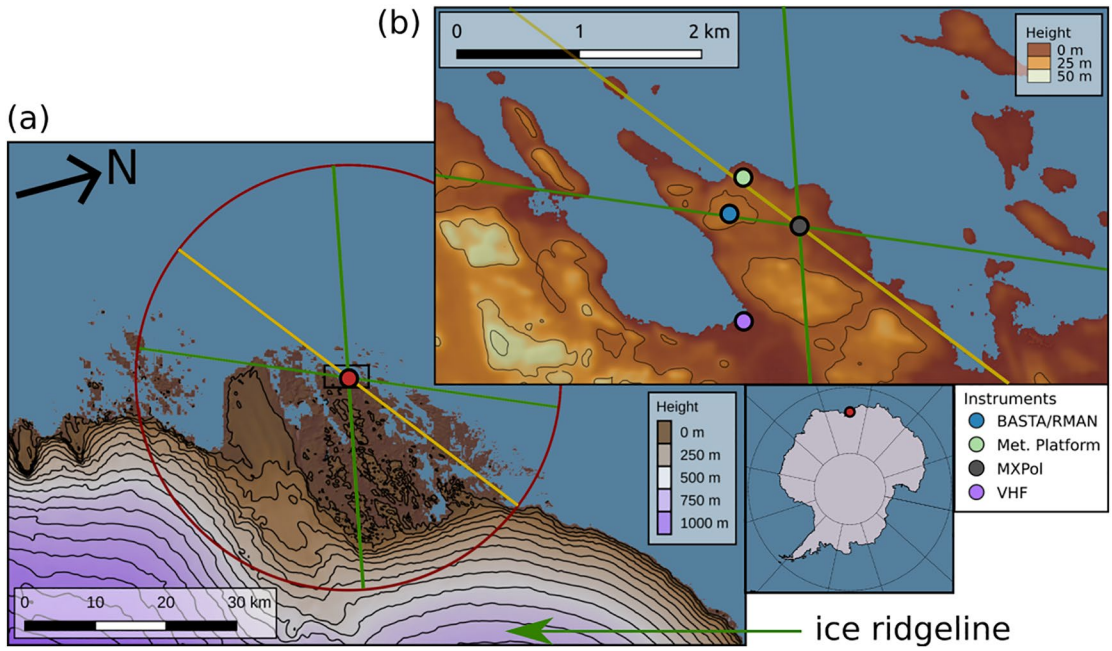

Figure 1. Topography of (a) the Vestfold Hills and (b) Davis station. The colored lines show the range height indicators (RHIs) of MXPol, the yellow one corresponds to the RHI at 52° azimuth. The red circle shows the extent of the plan position indicator. The locations of the instruments are shown in (b). The colored shadings correspond to altitude in m a.s.l. The altitude contours of (a) are shown every 100 m and of (b) every 20 m. The main ice ridgeline responsible for the generation of OGWs is shown with an arrow. The blue corresponds to altitudes ≤ 0 m a.s.l.

The Amery Ice Shelf starts at about 120 km to the south-west of Davis (Figure 2). The main ice ridge responsible for the generation of OGWs (Alexander & Murphy, 2015; Alexander et al., 2017) is located about 80 km to the north-east of Davis and reach about 1,000 m a.s.l. at the end of its steepest part (visible in Figures 1 and 2). In January 2019 only scattered patches of sea-ice were present around Davis. At this time of the year, solar noon is at about 07:00 UTC. In this study, we focus on the data collected by an X-band Doppler dual-polarization (polarimetric) radar (hereafter MXPol), a W-band Doppler cloud profiler (hereafter, BASTA), a Raman lidar (hereafter, RMAN), and a very-high frequency wind-profiling radar (hereafter, VHF). In addition, we use radiosounding measurements (12-hourly resolution) and wind, temperature, pressure, and humidity measurements from an automatic weather station (AWS) located at Davis and managed by the Australian Bureau of Meteorology.

2.1. Instrumentation

2.1.1. X-Band Polarimetric Radar: MXPol

MXPol operates at 9.41 GHz with a typical angular sampling resolution of 1° and a range resolution of 75 m (see Schneebeli et al., 2013, for more details). The sensitivity at 5,000 m range is of 0 dBZ (see Gehring et al., 2021, for the relation between sensitivity and range for MXPol). Only the data up to about 28 km range are saved, since the decrease in sensitivity and increase in sampling volume make the further gates less relevant for microphysical studies. The scan cycle was composed of three hemispherical range height indicators (RHIs, i.e., a cross-section) at 23°, 52°, and 101° azimuth. The 23° RHI passes above the location of BASTA and RMAN, the 52° RHI (yellow line in Figure 1) above a meteorological platform with other instruments not used in this study (Met. Platform in Figure 1), and the 101° RHI is towards the ice sheet. The cycle was completed by one plan position indicator (PPI) at 4° elevation (red circle in Figure 1) and one PPI at 90° elevation (hereafter vertical PPI). The 52° and 101° RHIs, and the 4° PPI have an unambiguous Doppler velocity of 39 m s^{-1}, while it is 11 m s^{-1} for the 23° RHI and the vertical PPI. The scan cycle had a 5 min duration and was repeated indefinitely. The main MXPol variables used in this study are the equivalent reflectivity factor (hereafter simply referred to as reflectivity) at horizontal polarization Z_H (dBZ), the differential reflectivity Z_{DR} (dB), and the spectral power (dBm).

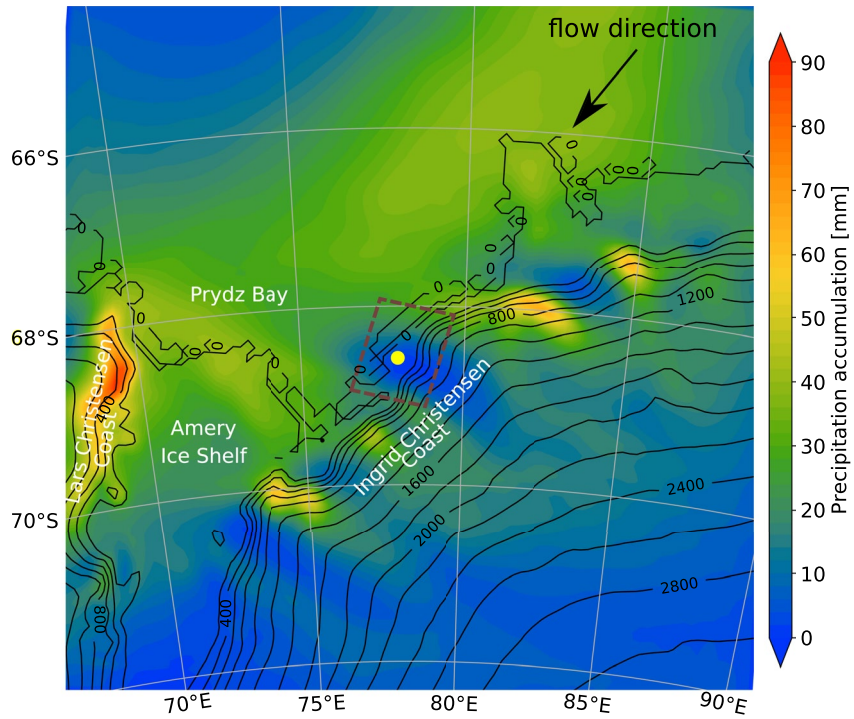

Figure 2. Precipitation accumulation (shading) from the Weather Research and Forecasting 9-km resolution domain from 00:00 UTC on 08 January to 12:00 UTC on 10 January 2019 and topography (black contours, labels in m a.s.l.).The yellow dot shows the location of Davis, the brown rectangle represents the domain shown in Figure 1a, the arrow shows the main wind direction at about 1,500 m a.s.l. during the event.

Z_{DR} has been calibrated by subtracting a time-dependent offset from the original Z_{DR} field, according to the algorithm described in Ferrone and Berne (2021). Following the criteria described in the article, only the region between 1,067 m and 3,681 m above the radar has been extracted from the vertical PPIs (2,932 over the whole campaign) and considered suitable for calibration purposes. The median Z_{DR} values from this vertical profile have been used as input for an ordinary kriging interpolation. The median Z_{DR} offset of the 6,495 RHI and PPI scans (restricted to precipitation periods) is 0.53 dB and the interquartile range is 0.03 dB, showing that the Z_{DR} offset was stable in time.

During the 23° RHI and vertical PPI, the full Doppler spectrum at 0.17 m s^{-1} resolution was retrieved. A semi-supervised hydrometeor classification algorithm (Besic et al., 2018) was applied on the polarimetric variables. We use its de-mixing product, which estimates the proportions of hydrometeor classes within one radar volume, allowing us to study mixtures of hydrometeors. More specifically, we will show the de-mixing classification of all RHIs for horizontal distances greater than 6 km and excluding elevation angles between 45° and 135°.

2.1.2. W-Band Cloud Profiler: BASTA

BASTA is a vertically pointing, single-polarization, frequency modulated-continuous wave Doppler cloud radar operating at 95 GHz, with a beamwidth of 0.4° (Delanoë et al., 2016). The radar operates on a 12 s cycle, based on four 3 s modes using different range resolutions (ranging from 12.5 to 100 m), corresponding to different Nyquist velocities and minimum detectable signal. The final product used in this study merges the four modes to provide 12 s resolution, 25 m vertical resolution profiles of reflectivity and Doppler velocity. BASTA has been calibrated following the procedure outlined in Protat et al. (2019), using statistical comparisons with T-matrix 95 GHz calculations from optical disdrometer observations (Klepp et al., 2018) and with a micro rain radar (MRR-PRO) 24 GHz vertically pointing radar observations (Klugmann et al., 1996) collected during the second phase of the Clouds, Aerosols, Precipitation, Radiation, and atmospherIc Composition Over the southeRN ocean experiment (Mace & Protat, 2018; McFarquhar et al., 2021), which took place just before the PLATO campaign. The consistency of all radar measurements of PLATO has also been established to be better than 1 dB by statistically comparing MXPol, MRR-PRO and BASTA observations collected during PLATO.

To compute the dual-frequency ratio (DFR) of reflectivity at X- and W-bands, vertical profiles of Z_H were extracted from all MXPol's RHIs for elevation angles between 89° and 91°. Since, MXPol is located about 600 m from BASTA, we decided to extract from the RHIs the vertical profiles above MXPol, rather than above BASTA, since the latter will suffer from a different viewing angle with respect to BASTA vertical profiles, which would influence the DFR. This timeseries of X-band reflectivity profiles (Z_X) can then be compared to the W-band reflectivity from BASTA (Z_W): both Z_X and Z_W profiles are binned to a common (time, height) grid with a time-step of 10 min and a height resolution of 50 m, which corresponds to two scan cycles of MXPol and two range gates of BASTA. The DFR is then computed as $Z_X - Z_W$, where Z_X and Z_W are in dBZ and hence the DFR is in dB. The principle of multi-frequency radar techniques was already introduced by Atlas and Ludlam (1961) and was used by Eccles and Atlas (1973) and Carbone et al. (1973) to detect hail. Later, Matrosov (1998) proposed a method based on dual-frequency radar measurements to measure snowfall rate. In essence, the principle of dual-frequency techniques is based on the fact that hydrometeors have different backscattering properties at the two frequencies: for the lower frequency the scattering is well described by the Rayleigh approximation, while the higher frequency will be in the resonance scattering regime (sometimes referred to as the Mie regime) for the hydrometeors of interest. In our case, snowflakes essentially remain in the Rayleigh regime at X-band, while they transition to the Mie regime at W-band as they grow in size. This leads to a plateau or a decrease in Z_W. The DFR hence reflects the median size of snowflakes and exhibits a sharp increase when processes, such as aggregation, lead to a rapid increase in snowflake size.

2.1.3. Raman Lidar: RMAN

RMAN (Leosphere RMAN-511) is a vertically pointing cloud-aerosol mini-Raman lidar measuring elastic backscatter and depolarization ratio at 355 nm, with a typical range resolution of 15 m and temporal resolution of 35 s (Royer et al., 2014). While, the RMAN system also includes a Raman scattering channel, the sensitivity of the system is such that long integration times in cloud-free tropospheric air are used for calibration (Alexander & Protat, 2019). From these lidar observations, cloud thermodynamic phase (liquid, ice, supercooled liquid water, and mixed-phase) is estimated first from the lidar backscatter and depolarization ratio using the algorithm described in Alexander and Protat (2018), then refined using cloud radar observations following Noh et al. (2019). In this study, we will only use the supercooled liquid water (SLW) category of this cloud classification.

2.1.4. Wind-Profiling Radar: VHF

The Davis VHF wind-profiling radar is a 55 MHz system consisting of 144-antenna main array with a one-way beamwidth of about 7°. Doppler radial velocities are obtained in the vertical, north, and east directions (with the off-vertical beams pointing at a 14° zenith angle), cycling every 6 min (Alexander et al., 2017). The vertical range resolution is 500 m and data are acquired from about 1,500 m a.g.l. to the lower stratosphere. Alexander et al. (2017) validated horizontal wind measurements from the same site (Davis) and the same VHF radar used in this study against colocated radiosoundings from February 2014 to February 2016. They showed a very good agreement with a correlation coefficient of 0.95 and a bias of 0.36 m s^{-1}.

2.2. WRF Simulations

We carried out numerical simulations using the version 4.1.1 of the WRF model. The simulation configuration has been developed for precipitation and cloud studies in Antarctica (Vignon, Besic, et al., 2019) and can be described as follows. WRF is run with a downscaling approach with a parent domain of 27 km resolution containing three (one-way) nested domains (Figure 3) with 9, 3, and 1 km resolution centered over Davis station. The topography and the so-called "land-use" surface conditions are from the 1-km resolution Reference Elevation Model of Antarctica data set (Howat et al., 2019) and from the AntarcticaLC2000 data set respectively. The WRF-compatible files have been built by Gerber and Lehning (2020) and they show substantial improvements compared to the standard WRF forcing files used for Antarctica (which exhibited no topographical information over the Vestfold Hills). The lateral forcings, the sea ice cover, the sea surface temperature and the initial conditions are from the ERA5 reanalysis (Hersbach et al., 2020). To ensure a realistic large-scale dynamics throughout the simulation time and to allow for a concomitant comparison between simulations and observations, the 27-km resolution domain has been nudged above the boundary layer towards ERA5 reanalysis for zonal and meridional wind with a relaxation time scale of 6 h. The 96-level vertical grid as well as the physical package employed are

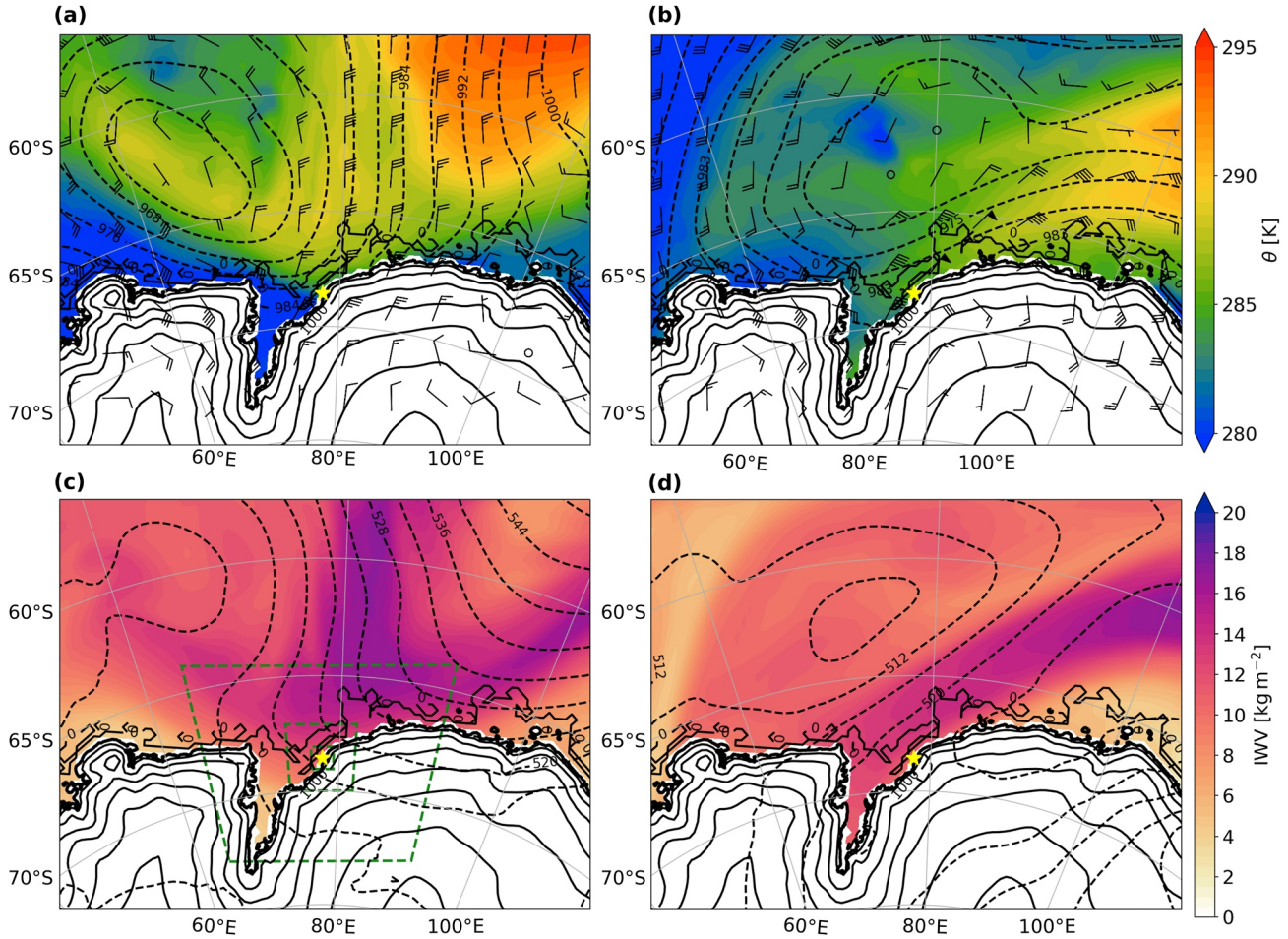

Figure 3. Synoptic maps from the Weather Research and Forecasting (WRF) domain at 27-km resolution at 09:00 UTC 08 January 2019 (a,c), and 00:00 UTC 10 January 2019 (b,d). Panels (a) and (b) show potential temperature (shading in K) and wind (barbs following meteorological standard notation) at 800 hPa, and mean sea level pressure (dashed contours, labels in hPa). Panels (c) and (d) show integrated water vapor (shading in kg m^{-2}) and geopotential height at 500 hPa (dashed contours, labels in decameter). The green dashed boxes in (c) show the extent of the WRF domains at 9, 3, and 1 km resolution (from the largest to the smallest domain respectively). The yellow stars show the location of Davis on the Ingrid Christensen Coast on the eastern side of Prydz Bay. The Lars Christensen Coast is on the western side of Prydz Bay.

the same as in Vignon et al. (2021). In particular, the vertical grid has been specifically refined in the mid-troposphere to ensure a proper representation of frontal mixed-phase clouds and the Morrison 2-moment microphysical scheme (Morrison et al., 2005) has been modified with a new ice nucleation parameterization adapted to the low concentrations of ice nuclei particles observed in the atmosphere off the Antarctic coasts. The other physics options include the new version of the Rapid Radiative Transfer Model for General Circulation Models (Iacono et al., 2008) radiation scheme for longwave and shortwave spectra, the Noah land surface model (Niu et al., 2011) with adaptations by Hines and Bromwich (2008) and the Mellor-Yamada-Nakanishi-Niino planetary boundary layer scheme (Janjić, 1994) coupled with its associated surface layer scheme. The Kain-Fritsch cumulus scheme (Kain & Fritsch, 1990) is also activated for the 27-km resolution domain. Simulations start at 00:00 UTC on 07 January 2019 corresponding to a 24 h spin-up time before the arrival of the first clouds above Davis.

3. Synoptic Evolution and Precipitation Distribution

At 00:00 UTC on 08 January 2019 a potential vorticity (PV) cutoff is located to the north of Davis (Figure 4) and is associated with a surface cyclone. This system advects moisture polewards on its eastern flank, as can be seen by the narrow filament of large IWV, up to 15 kg m^{-2} extending meridionally over thousands of kilometers and resembling an AR. As explained in Gorodetskaya et al. (2014), the thresholds used to define ARs in the

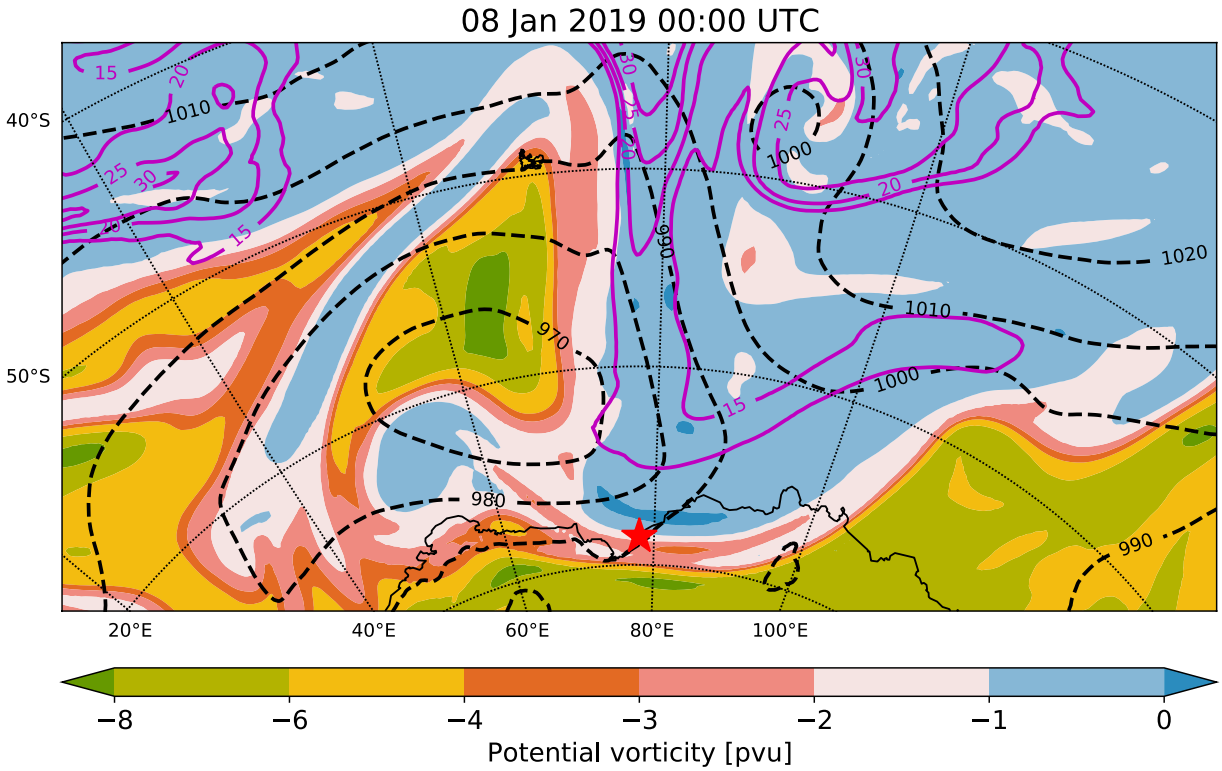

Figure 4. Synoptic situation at 00:00 UTC 08 January 2019 from ERA5 data. Potential vorticity (shading in potential vorticity unit (pvu) = 10^{-6}) at the 315 K isentrope, mean sea level pressure (dashed contours, labels in hPa), and integrated water vapor (magenta contours, labels in kg m^{-2}). The red star shows the location of Davis.

midlatitudes (e.g., Ralph et al., 2004; Ralph et al., 2006) cannot be applied to the much drier and colder Antarctic environment. For this reason, Gorodetskaya et al. (2014) proposed a threshold on IWV based on the zonal mean saturated IWV, which is consistent with the idea that ARs are outstanding moisture transport compared to the zonal mean (Zhu & Newell, 1998). Alternatively, Wille et al. (2021) developed an AR detection algorithm based on temporal percentiles of IWV at each location. Based on this algorithm, the 08–10 January 2019 event over Prydz Bay qualifies as an AR (J. Wille, personal communication).

The warm front of this extratropical cyclone is visible as a sharp temperature gradient to the north of Davis, while a cold air pool is located ahead over Prydz Bay (Figure 3a). The thermal wind at this sharp temperature boundary leads to a barrier wind (van den Broeke & Gallée, 1996), which can be noticed in the wind fields of Figure 3a. Once the cold air pool has been eroded by advection and mixing of warm air associated with the passage of the warm front, the barrier wind is not present anymore (Figure 3b) after about 00:00 UTC on 09 January. This together with a north-easterly flow at all heights after 07:00 UTC on 09 January (Figures 5b and 6d) as the surface cyclone moves eastwards allows the atmospheric river to make landfall on the Lars Christensen Coast, discharging its moisture on the steep slopes of the ice sheet (IWV in Figure 3d).

With the passage of a warm front and the presence of an AR, favorable synoptic ingredients for intense precipitation over Prydz Bay are present. Figure 2 shows that there is indeed significant precipitation accumulation of up to 85 mm in 60 h. However, the spatial distribution of precipitation is very heterogeneous and shows two striking features. First, the largest accumulation is on the Lars Christensen Coast, where most of the AR makes landfall on the steep slope at the northernmost part of the coast. Second, on the Ingrid Christensen coast (i.e., where Davis is located) some patterns of precipitation accumulation appear with the maxima (minima) located windward (leeward) of the main ridges. Most of all, Davis is located in the broadest dry area in the lee of a ridge.

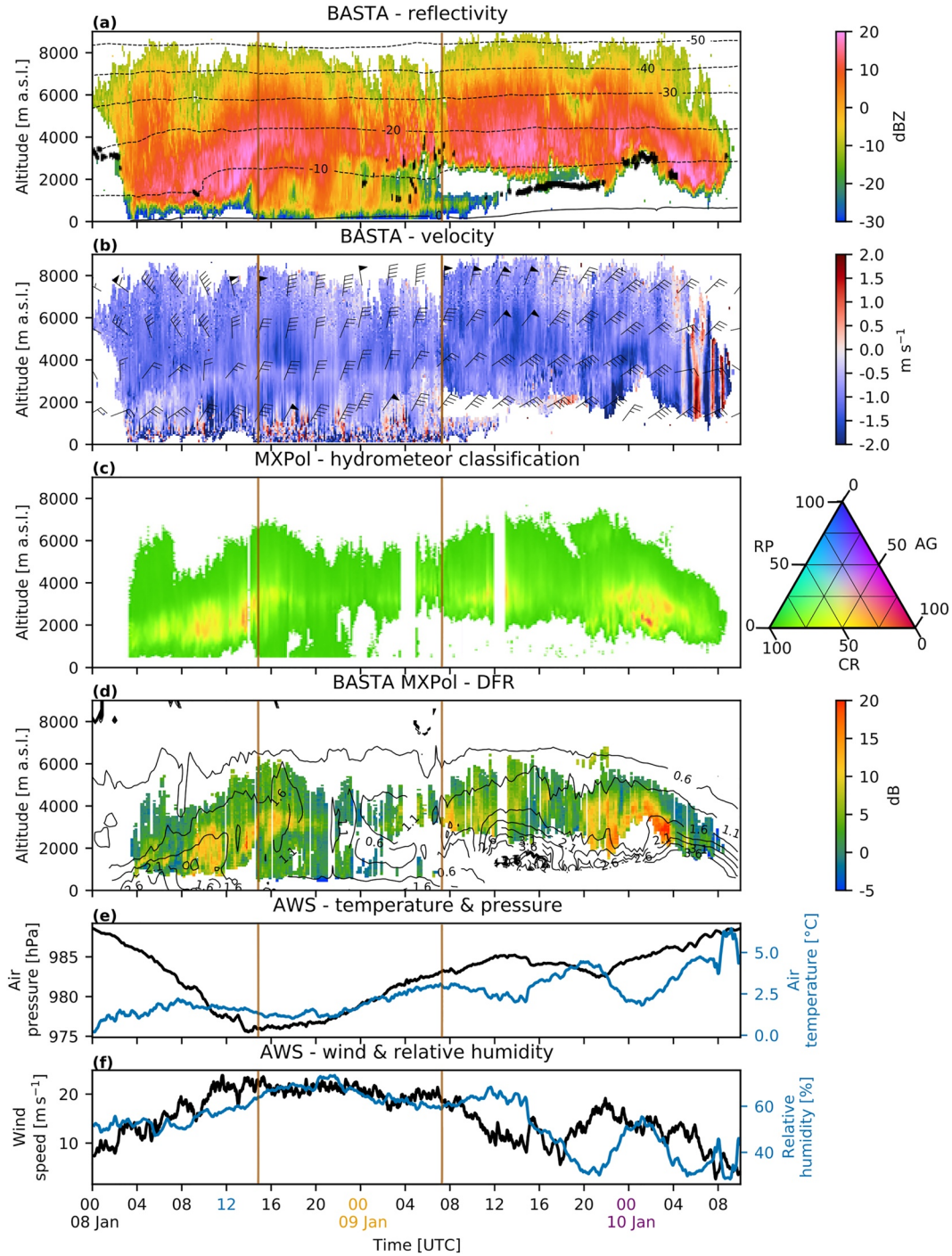

Figure 5. Time series from 00:00 UTC 08 January to 10:00 UTC 10 January 2019 of (a) reflectivity of BASTA (shading), isotherms from the Weather Research and Forecasting (WRF) model (black contours, labels in°C) and supercooled liquid water from RMAN cloud classification data (black shading), (b) mean Doppler velocity from BASTA (shading, defined positive upwards), horizontal wind from the very high frequency radar (barbs following meteorological standard notation), (c) hydrometeor classification based on all MXPol range height indicators (shading, see Section 2.1.1). The proportion (in %) of aggregates, crystals, and rimed particles can be read on the edges of the triangle by following the direction of the ticks. (d) dual-frequency ratio from MXPol and BASTA (shading, see Section 2.1.2) and D_{mean} from WRF (contours, labels in mm), (e) air temperature and pressure from the automatic weather station (AWS), and (f) wind speed and relative humidity with respect to ice from the AWS. The colors of the 00:00 and 12:00 UTC labels correspond to the radiosoundings shown in Figure 6.

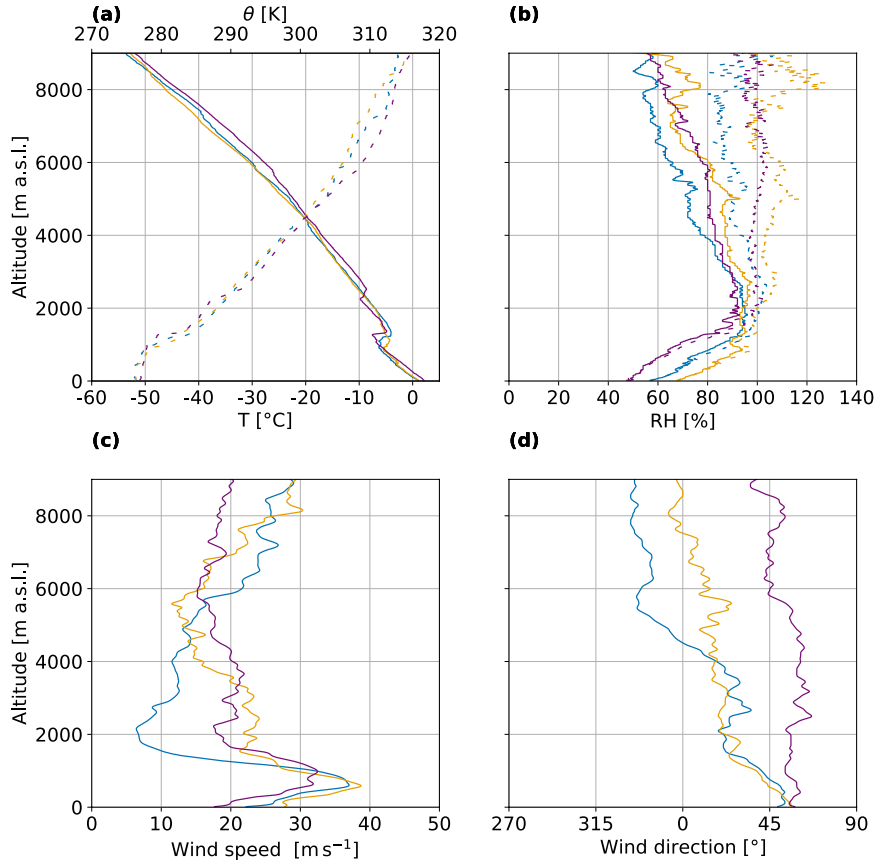

Figure 6. Radiosoundings launched at Davis station on 08 January at 12:00 UTC (blue), on 09 January at 00:UTC (yellow), and on 10 January at 00:00 UTC (purple) of (a) temperature (T, solid lines) and potential temperature (θ, dashed lines), (b) relative humidity with respect to liquid (solid lines) and ice (dashed lines), (c) wind speed, and (d) wind direction.

4. The Evolution of Snowfall and Orographic Gravity Waves Over Davis

In this section, we analyze the evolution of the local dynamics and snowfall microphysics over Davis to understand which processes led to the dry area over the Vestfold Hills, despite the intense large-scale moisture advection during this event. We divide the event into three distinct phases: phase I features the passage of the warm front and sublimation below 1,000 m, phase II corresponds to the period where light precipitation reaches Davis, and phase III is characterized by intense sublimation below about 2,000 m.

4.1. Phase I: Passage of the Warm Front and Trapped Orographic Gravity Waves, 02:00–15:00 UTC 08 January 2019

At 00:00 UTC on 08 January pre-frontal clouds are present over Davis and by 04:00 UTC a nimbostratus cloud with reflectivity values of up to 15 dBZ is extending to almost 8,000 m (Figure 5a). At 12:00 UTC the air is subsaturated w.r.t. ice below 1,800 m a.s.l (blue dashed line in Figure 6b) and snowfall sublimates completely before reaching the ground. Advection away from the radar volume by the strong winds around 1,000 m a.s.l. can be excluded, since this sublimation is also observed in MXPol RHIs (Figure 9a) over distances greater than possible by advection. In this dry layer, turbulence can be seen as small regions of up- and downdrafts in BASTA mean Doppler velocity before 14:00 UTC below 2,000 m. The passage of the warm front can be seen as a sharp increase of the − 10 °C isotherm altitude at 10:00 UTC (Figure 5a) and is associated with strong turbulence (Figure 5b), a faster decrease of pressure (Figure 5e) and increase in wind speed (Figure 5f).

The sharp temperature gradient between the cold air pool over Prydz Bay and the warm front (Figures 3a and 7a) causes a strong thermal wind which can be clearly seen before 10:00 UTC with backing winds with height

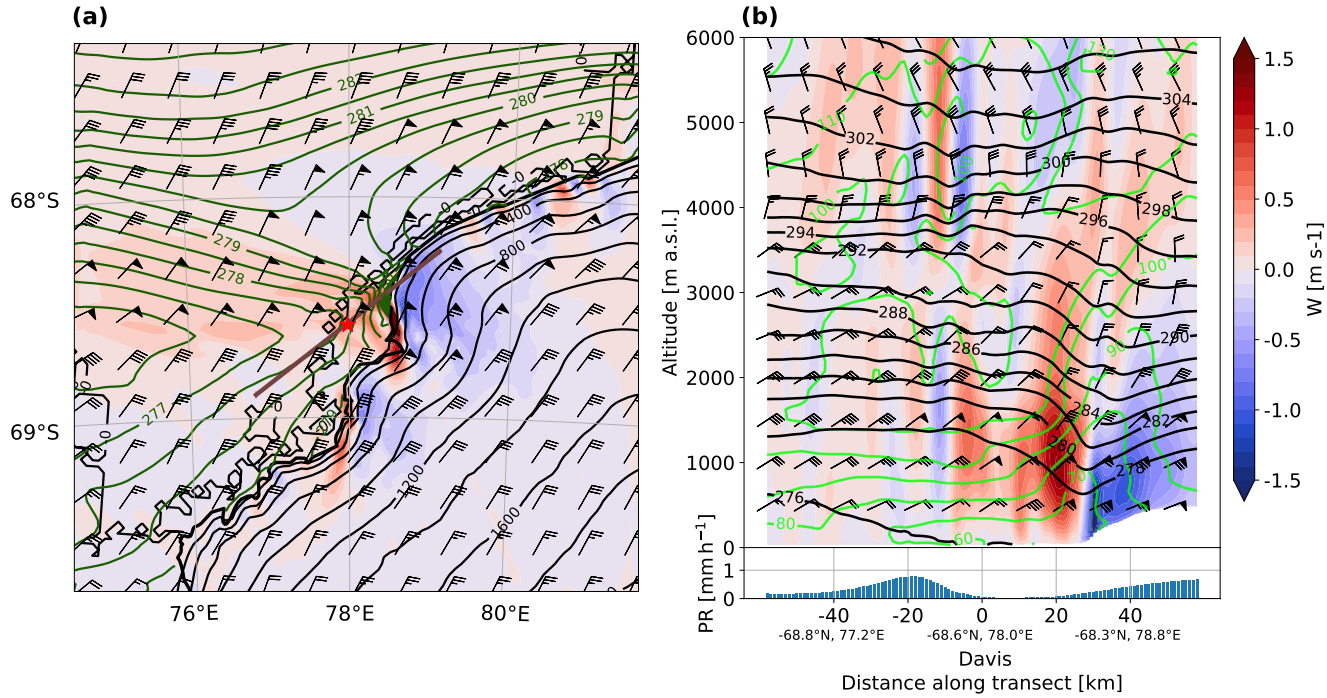

Figure 7. Output from the Weather Research and Forecasting model on 08 January 2019 at 09:00 UTC. (a) Map of the 3-km resolution domain of vertical wind velocity (shading in m s^{-1}), horizontal wind (barbs following meteorological standard notation), and potential temperature (dark green contours) at 850 hPa (about 1,200 m a.s.l.). The black contours show the topography (labels in m a.s.l.) and the red star the location of Davis. (b) cross-section of the 1-km resolution domain, corresponding to the brown line in (a), of vertical wind velocity (shading in m s^{-1}), potential temperature (black contours, labels in K), relative humidity w.r.t. ice (green contours, labels in %) and horizontal wind (barbs following meteorological standard notation) and precipitation rate along the cross-section (blue bars in mm $^{-1}$).

(Figure 5b), consistent with warm air advection in the Southern Hemisphere. The barrier wind (Figure 3a) resulting from this temperature gradient deflects the moist flow such that the Lars Christensen Coast is protected from intense precipitation at this early stage of the event. The thermal wind provides the ideal orientation (north-easterly) for the generation of OGWs along the Ingrid Christensen Coast, while the warm front produces large-scale lifting and likely enhanced the updrafts in the OGWs (Figure 7a). The flow-topography interaction leads to a foehn effect in the lee of the ridge with clear isentropic drawdown (e.g., Damiens et al., 2018), negative vertical velocity, and a relatively dry air tongue extending even downstream of Davis station (Figure 7b). A hydraulic jump at the base of the ice plateau is also evident in Figure 7b and manifests as a strong updraft extending up to 3,500 m. Note that the Vestfold Hills correspond to the dry zone directly in the lee of the ridge, while most of the precipitation fall upstream of the ridgeline and downstream of Davis (bars in Figure 7).

There is a layer with enhanced static stability between 3,500 and 4,000 m downstream of Davis (as indicated by the closer isentropes in Figure 7b), the vertical wind shear below this layer is weak and the thermal wind is mostly present inside and above it, with wind shifting from east-northeasterly at 3,000 m to northerly at 4,000 m. This layer of enhanced static stability is partly due to the hydraulic jump and subsequent flow separation, which makes the isentrope downstream of the jump and below 1,800 m move apart, leading to a boundary layer destabilization (Vignon et al., 2020). OGWs are trapped at low levels downstream of the jump (Figure 7b), but extend vertically up to the layer of increased static stability (~3,500 m). This corresponds to the case of waves propagating on a temperature inversion located close to the surface (i.e., ~1,000 m, Figure 6a) as described in Sachsperger et al. (2017).

From a microphysical perspective, two main zones of aggregation can be identified during the event: (a) from 08:00 to 16:00 UTC on 08 January between 1,000 and 4,000 m, and (b) from 20:00 UTC 09 January to 04:00 UTC 10 January between 2000 and 4,000 m. While the latter belongs to Phase III and will be further discussed in Section 4.3, we discuss their common features here. In both cases the maxima of DFR are collocated with zones dominated by aggregates in MXPol hydrometeor classification and with maxima of mean particle mass diameter (D_{mean}) from WRF (Figures 5c and 5d, respectively). Note that since MXPol hydrometeor classification

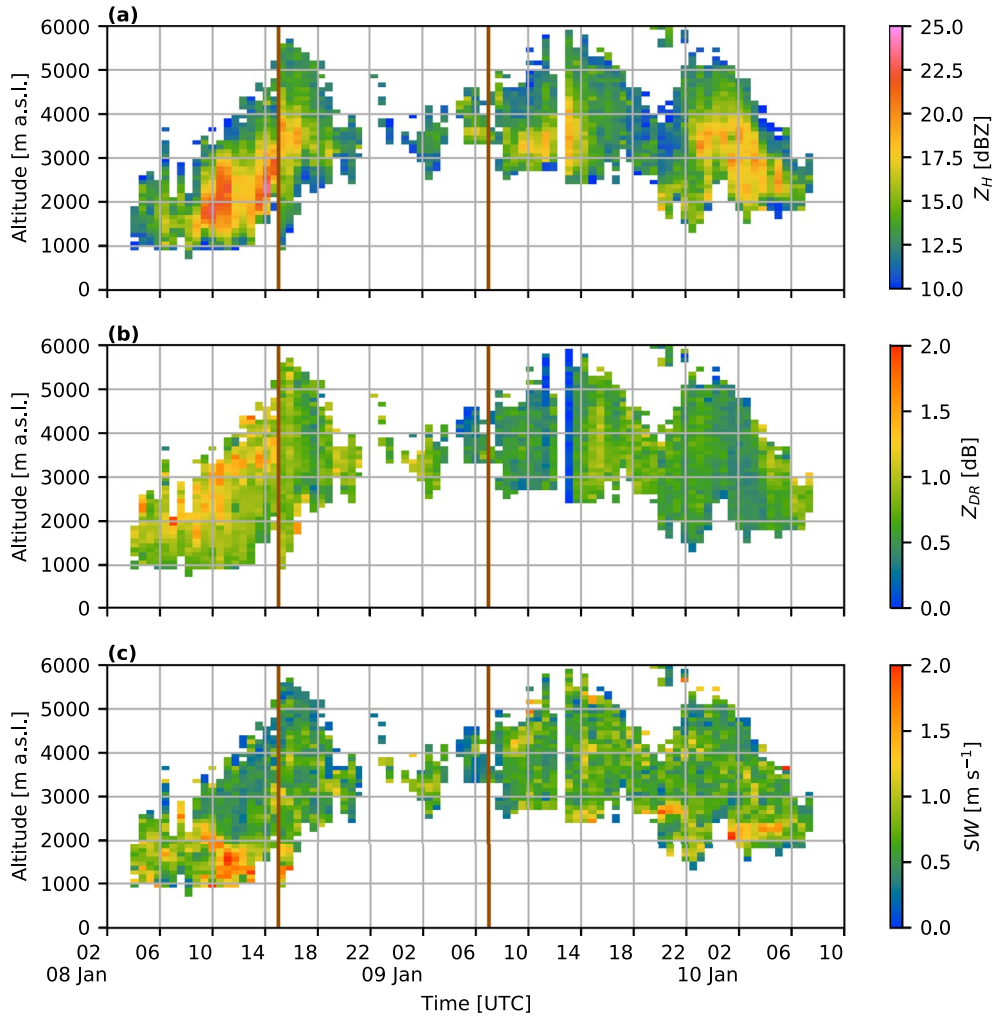

Figure 8. Time series of (a) MXPol Z_H, (b) Z_{DR}, and (c) spectral width from 02:00 UTC 08 January to 10:00 UTC 10 January. The profiles were extracted from the range height indicators at 23° and 52° elevation from 6,000 to 10,000 m range and for elevation angles greater than 135°.

(Figure 5c) shows data from all RHIs at horizontal distances greater than 6 km, the observed volumes are not comparable with those at vertically pointing mode (compare Figures 5a and 5c where aggregates are identified while no signal is present in BASTA measurements at around 02:00 UTC on 10 January). These aggregation zones are located at temperatures above − 20 °C (Figure 5a), which represent favorable conditions for significant aggregation (Connolly et al., 2012; Hobbs et al., 1974; Phillips et al., 2015). Although the DFR and MXPol hydrometeor classification are not totally independent (they both use Z_X), the other variables used clearly point towards aggregation and/or riming (minimum of Z_W due to Mie scattering regime, visible in Figure 5a, which strongly contributes to the maximum of DFR, and low Z_{DR} in Figure 8b interpreted as aggregates in MXPol classification). The simulation of D_{mean} from WRF is qualitatively consistent with the DFR in the aggregation layer (Figure 5d) and shows that WRF is able to reproduce the zones of dominant aggregation. The high DFR and low Z_{DR} signatures could also indicate riming, which likely also occurred since SLW is visible at around 2,000 m both in the radiosoundings (Figure 6b, yellow line) and in the RMAN cloud classification, whenever the signal is not totally attenuated below 2,000 m (Figure 5a, black shading). While triple frequency allows to distinguish between aggregation and riming (Battaglia et al., 2020; Kneifel et al., 2015; Tridon et al., 2019), we argue that the hydrometeor classification can also discriminate aggregates from substantially rimed particles. Indeed, Figure 5c shows little proportion of very rimed particle, whereas dry to moderately rimed aggregates are very frequent in the lower part of the clouds. While riming probably occurs locally in space and time when SLW is present in the cloud, we hereafter focus our analysis on the aggregation process, which seems to occur during most of the event.

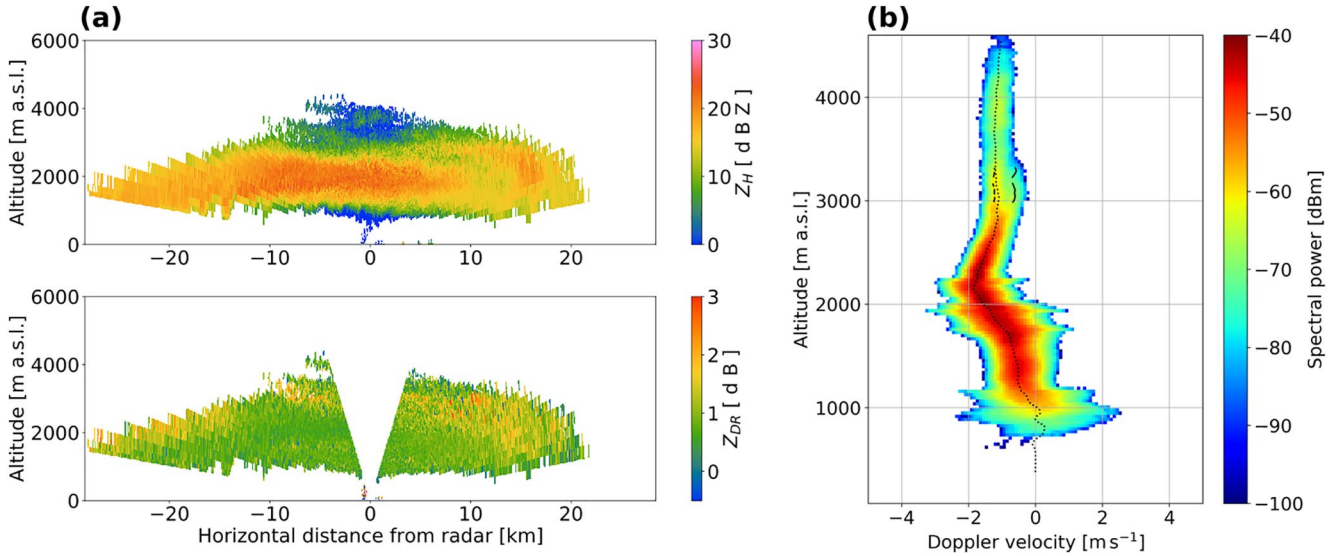

Figure 9. (a) MXPol range height indicator at 52° azimuth (yellow line in Figure 1) at 09:27 UTC 08 January of Z_H, and Z_{DR}. (b) MXPol Doppler spectrogram averaged over a vertical plan position indicator at 09:24 UTC 08 January. The dotted line shows the mean Doppler velocity, the dashed and solid lines show, if present, the velocity of the first and second mode, respectively.

Figure 8 shows a layer of enhanced Z_{DR} varying between 2000 and 4,000 m during Phase I. This layer represents the end of depositional growth and the start of aggregation. Below this layer, Z_{DR} decreases drastically, while Z_H increases and reaches its maximum of 22 dBZ at 1,500 m. This is due to intense aggregation taking place from 3,000 to 1,200 m, as can also be observed by the increase in aggregates' proportion in Figures 5c and is consistent with DFR observation and D_{mean} simulation of WRF in Figure 5d. Figure 9a shows an RHI representative of Phase I. The layers of enhanced Z_H and Z_{DR} are clearly visible at 2,000 and 3,000 m, respectively. The aggregation below about 2,500 m could be favored by the turbulence generated by the strong vertical motions within the OGWs (Figure 7b) and then advected downstream to Davis. This turbulence can be seen as an increases in spectral width below 2,500 m in Figures 9b and 8c during phase I. Maxima of turbulent kinetic energy from WRF simulations (not shown) were observed within the OGWs, suggesting that turbulence is produced by the intense vertical motions visible in Figure 7b. Other factors could favor aggregation, such as temperature and relative humidity, which determine the ice habit (Bailey & Hallett, 2009). For instance, the branches of dendrites make them more likely to interlock than the flatter surfaces of plates. The temperature range at which aggregation is observed (− 15 °C to − 10 °C) corresponds to planar crystal growth (Libbrecht, 2005), however dendritic crystal growth requires liquid water saturation, which we did not observe in our case (Figure 6b). We conclude that the observed aggregation is more likely to be enhanced by the observed turbulence than by the presence of favorable ice habits. The Doppler spectrum shown in Figure 9 supports our microphysical interpretation: the depositional growth above 3,000 m leads to a slight increase in the magnitude of Doppler velocity and reflectivity, while the aggregation below 3,000 m causes a sharp increase in the same variables. When the aggregates enter the updrafts within the OGWs at 2,200 m, the magnitude of Doppler velocity decreases and the spectral width increases due to the turbulence. This could favor continuous aggregation and riming until 1,200 m, where the snowflakes sublimate. The vertical extent of the updraft as shown in this Doppler spectrum is consistent with the OGWs simulated by WRF and shown in Figure 7b.

In summary, the thermal wind enhanced by the cold air pool over Prydz Bay ahead of the warm front provides a favorable flow direction below 2,000 m for the generation of OGWs. A foehn effect manifesting as an isentropic drawdown in the lee of the ridge is followed by a hydraulic jump that favors the trapping of gravity waves downstream. The relatively dry foehn air that flows at low levels down to Davis station leads to total snowfall sublimation below about 1,500 m above the station and explains the dry area extending over the Vestfold Hills. The OGWs also affect the snowfall microphysics by providing ideal conditions for aggregation through the generation of updrafts and turbulence.

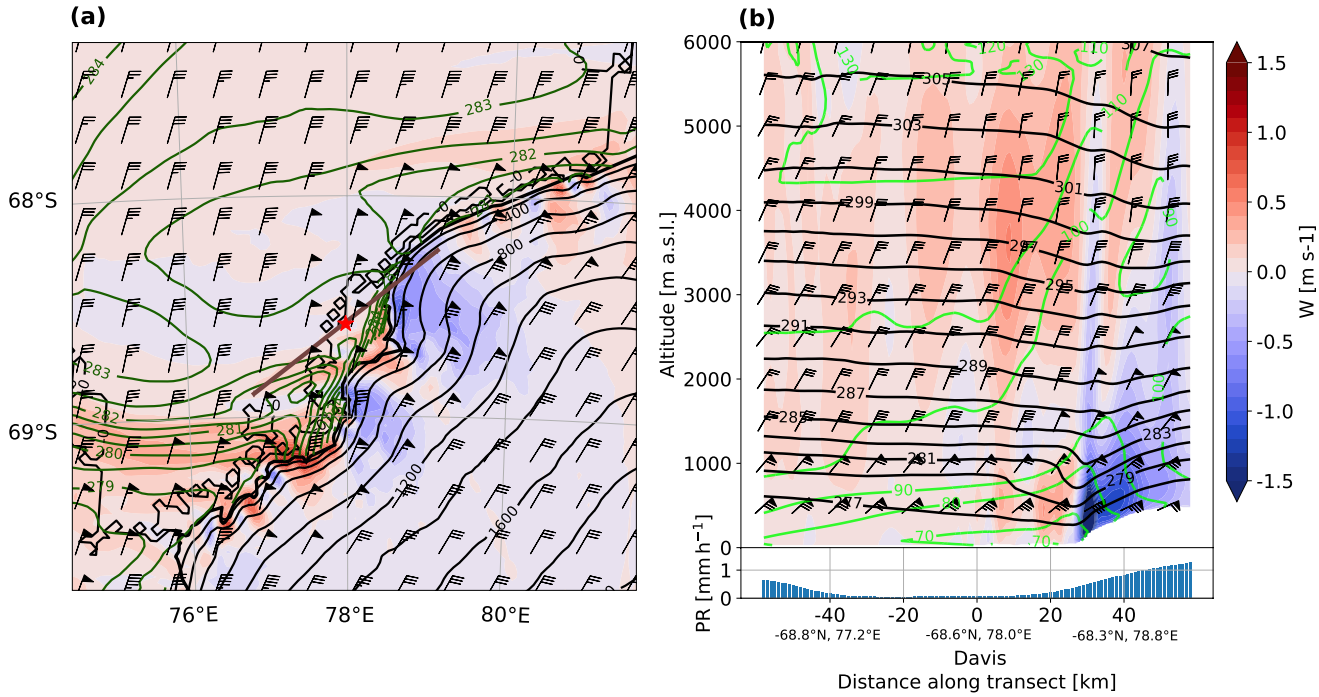

Figure 10. As for Figure 7 except at 18:00 UTC 08 January 2019.

4.2. Phase II: Northerly Flow and Light Precipitation at Davis, 14:00 UTC 08 January to 07:00 UTC 09 January 2019

As the warm front passes, the stable layer at around 4,000 m dissipates, the thermal wind weakens, and the synoptic flow becomes north-northeasterly (Figure 10a). As a consequence, winds are oriented more northerly at all heights (Figure 5b at 16:00 UTC 08 January). As can be seen in Figure 10a and a north-northeasterly flow will not impinge perpendicularly to the ridge located to the north-east of Davis, but rather to the ridge located further south where, the strongest OGWs are present. The collocation of the warm front with these intense OGWs, as during Phase I, suggests that it provides large-scale lifting enhancing the updrafts. Along with the absence of intense low-level OGWs over Davis, the foehn effect weakens (relative humidity increases and air temperature decreases, Figures 5e and 5f). The increase in relative humidity can be seen throughout the depth of the boundary layer (Figure 6b). It allows light precipitation to reach Davis between 14:00 UTC 08 January and 06:00 UTC 09 January. The absence of low-level trapped OGWs during Phase II coincides with much less aggregation than during Phase I. Indeed, the layer of aggregation is less intense and confined between 3,000 and 4,000 m before disappearing completely after 20:00 UTC 08 January (Figures 5c and 5d). The reflectivity values at both X- and W-bands are also weaker (Figures 5a and 5d). Although reflectivity is significantly lower during this period, snowfall reaches the ground since sublimation is less intense. While, the foehn effect is less pronounced during Phase II, it is enough to cause partial snowfall sublimation below about 2,000 m (Figure 5a).

The most intriguing radar signature during Phase II is the minimum of Doppler velocity observed around 3,000 m, in particular between 14:00 and 20:00 UTC on 08 January (Figure 5b). A careful investigation of the spectrograms from MXPol's vertical PPIs revealed that this minimum is due to an updraft varying between 0.5 and 1 m s^{-1}. Figure 11b shows an example of such a spectrogram, where a bimodality is present just above the updraft layer. Almost all spectrograms during the period where this minimum in Doppler velocity is observed featured both a decrease in the magnitude of the mean Doppler velocity and a bimodality. To ensure that this minimum in Doppler velocity is due to an updraft and not only to the contribution of the secondary mode in decreasing the magnitude of the mean Doppler velocity, we computed the velocity of the primary mode only (not shown), which revealed the same behavior as the mean Doppler velocity showed in Figure 5b. This updraft tends to broaden the spectrum and skew the distribution towards smaller magnitudes of Doppler velocity (Figure 11). The increase in spectral width is due to the turbulence in the updraft, similar to turbulence present in other summertime cloud

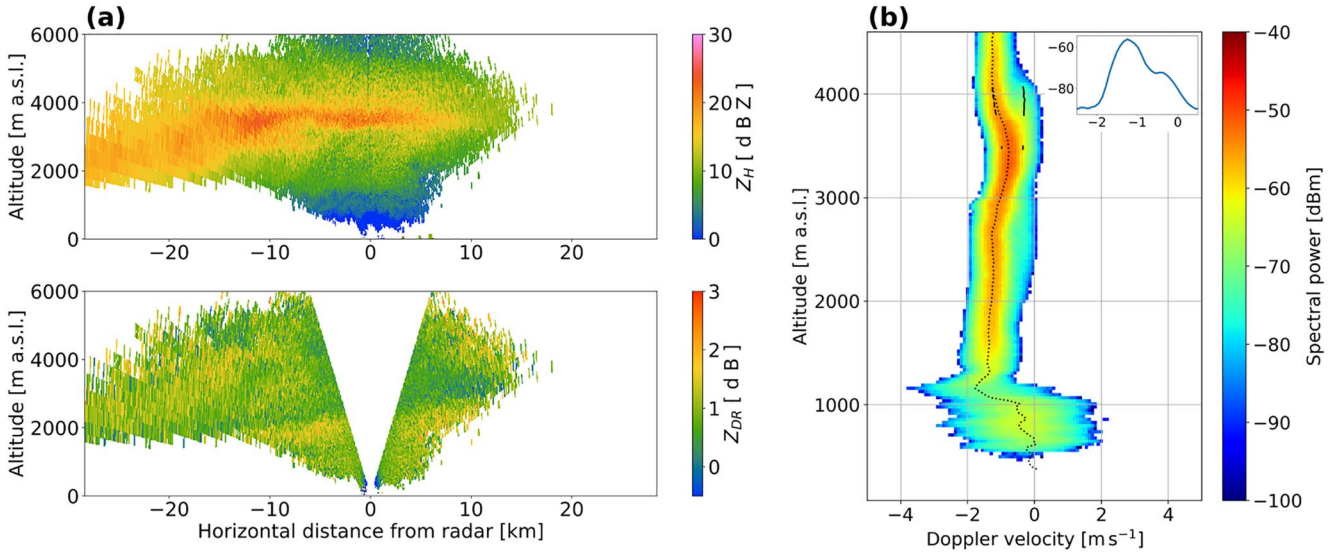

Figure 11. As for Figure 9 except at (a) 16:03 and (b) 16:10 UTC 08 January. The inset in (b) shows the corresponding spectrum at 3,976 m a.s.l., the *x*-axis is Doppler velocity in m s^{-1}, and the *y*-axis is spectral power in dBm.

systems which were observed by ship-based remote sensors near Davis and Mawson (650 km west of Davis, Alexander et al., 2021). Note that it is much lighter than the turbulence observed in the boundary layer below 1,000 m. The increase in skewness could be due to a size sorting effect by the updraft. The size sorting cannot however totally explain the bimodality, since it is unlikely to create such a discontinuity in the Doppler spectrum. We hypothesize that the bimodality is due to secondary ice production. While horizontal advection of ice and primary ice nucleation could also cause such a bimodality, we advocate that the former is not a plausible explanation for its persistence over several hours. The latter is unlikely to be a significant source of new ice particles, unless it occurs through freezing of SLW droplets, which is not supported by the radiosounding measurements (subsaturated conditions with respect to liquid at 4,000 m in Figure 6b), as suggested by Vignon et al. (2021). Also, Sotiropoulou et al. (2021) and Young et al. (2019) showed that the most important source of ice particles over the Antarctic coast likely originates from secondary ice production. We argue that collisional breakup of ice crystals (Takahashi et al., 1995; Vardiman, 1978) at the top of the updraft is a likely secondary ice mechanism to explain the observed bimodality. Sotiropoulou et al. (2021) showed that breakup could account for the enhanced number concentration of ice crystals often measured in Antarctic clouds (Young et al., 2019). They also showed that a minimum concentration as low as ~0.1 L^{-1} of primary ice crystals is sufficient. Considering the measured reflectivity during this event, the primary ice concentration is probably much above this threshold. Furthermore, for secondary ice production through breakup to be efficient, snowflakes have to be partially rimed. Despite the lidar signal being almost totally attenuated, some regions of SLW (black shading in Figure 5a) at around 3,000 m are visible during Phase II, suggesting that riming can at least partially occur. The MXPol hydrometeor classification however does not show significant occurrences of rimed particles during Phase II, likely due to its sensitivity to large rimed particles, which are not present here considering the low reflectivity values. Also, it requires a certain degree of riming for particles to be classified as rimed, which means that the crystals category can contain some rime. Moreover, photographs of snowflakes (only nine due to the strong wind) taken by a snowflake imager (not shown) during Phase II revealed the presence of small graupel particles, which confirm that SLW must have been present. Finally, Takahashi et al. (1995) showed that breakup was the most efficient at − 16 °C, which corresponds to the temperature at which we observe this bimodality (Figures 5a and 6a). Other secondary ice generation processes involving significant SLW amounts, such as rime splintering (so-called Hallett-Mossop process, Hallett & Mossop, 1974) and droplet shattering (Korolev & Leisner, 2020), are less likely to dominate here, since we have no evidence for the required SLW amounts at this height. In particular, the Hallett-Mossop process operates at temperatures between − 3 and − 8 °C whereas we observe this bimodality at a temperature of − 15 °C.

As to the origin of this updraft observed between about 3,000 and 4,000 m from 12:00 to 20:00 UTC, Figure 10b shows that a gravity wave train propagating downstream of the ice-ridge is present between 3,000 and 5,000 m

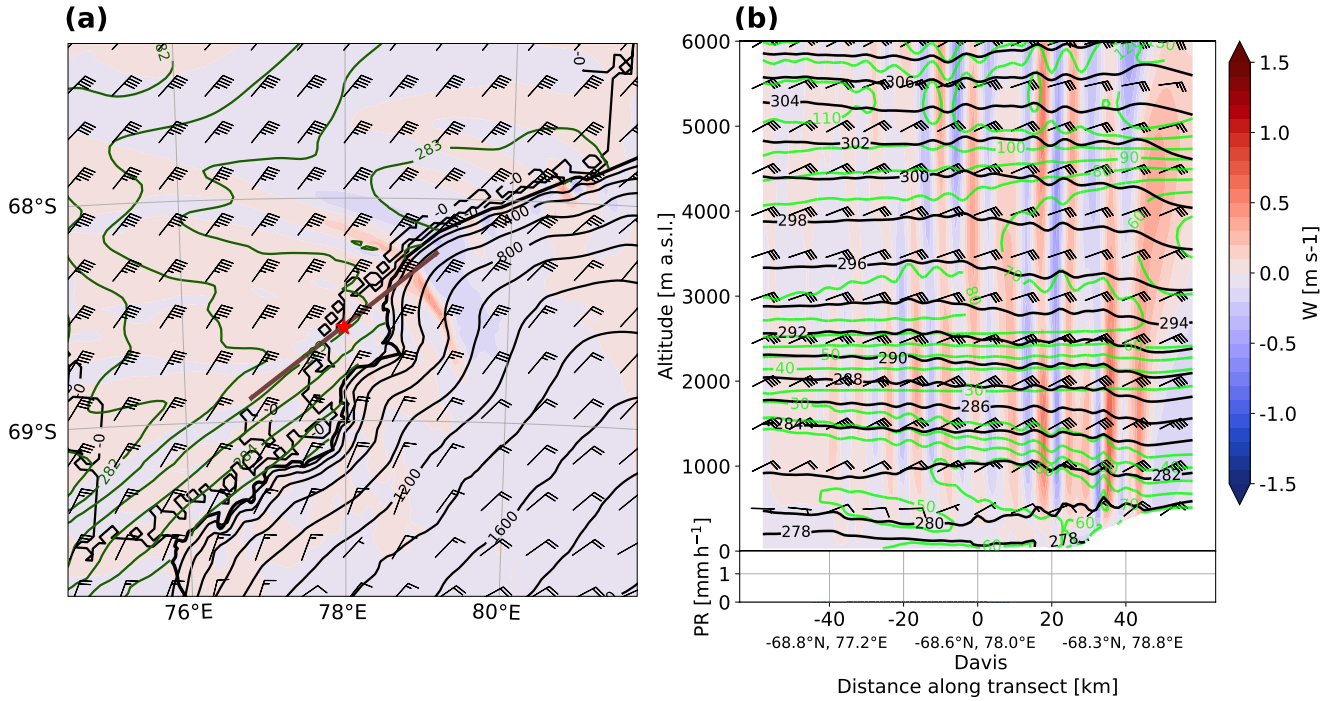

Figure 12. As for Figure 7 except at 07:00 UTC 10 January 2019.

above Davis. In particular, a maximum of vertical wind speed is observed above the Vestfold Hills at 3,500 m, which corresponds to the altitude at which the updraft is observed in the radar data (Figures 5b and 11b). This feature is quasi-stationary in the WRF simulation during the whole period where we observe the minimum in Doppler velocity in Figure 5b, suggesting that this updraft is probably due to the gravity wave train between 3,000 and 5,000 m shown in Figure 10. Schrom and Kumjian (2016) observed a similar minimum in Doppler velocity near the − 15 °C isotherm and hypothesized that the updraft could be induced by heating during depositional growth among other processes, which are thoroughly discussed in their study.

In summary, Phase II is characterized by a north-northeasterly flow at all heights, which prevents the formation of intense low-level OGWs as during Phase I and consequently the foehn effect is weaker and snowfall only partially sublimates. Nonetheless, quasi-stationary OGWs are present between 3,000 and 5,000 m and lead to a minimum in the magnitude of mean Doppler velocity and possibly secondary ice production.

4.3. Phase III: North-Easterly Flow and Nonstationary Orographic Gravity Waves, 07:00 UTC 09 January to 10:00 UTC 10 January 2019

Starting from 07:00 UTC on 09 January, OGWs, which propagate vertically further than during Phase I, formed at the base of the ice plateau 20 km upstream from Davis (not shown). At around 14:00 UTC temperature rises, while relative humidity decreases as the foehn effect intensifies again (Figure 5f). This coincides with winds below 4,000 m becoming increasingly easterlies (Figure 5b) due to the configuration of the upper-level low (Figure 3d). This north-easterly flow impinges the ridge upstream of Davis perpendicularly and generates a band of updrafts oriented along the ridge line (Figure 12a), similar to the case study of Alexander et al. (2017). Theses updrafts produce orographic clouds, which are clearly visible in the satellite image presented in Figure A1.

After 14:00 UTC, the air temperature is anti-correlated with the relative humidity (Figures 5e and 5f), which supports our hypothesis of a foehn wind event. Indeed, Kirchgaessner et al. (2021) showed that temperature and relative humidity are in antiphase during foehn events in the Antarctic Peninsula. The overall increase in temperature during the event is a combination of the passage of the warm front and of a foehn wind. The shorter phases

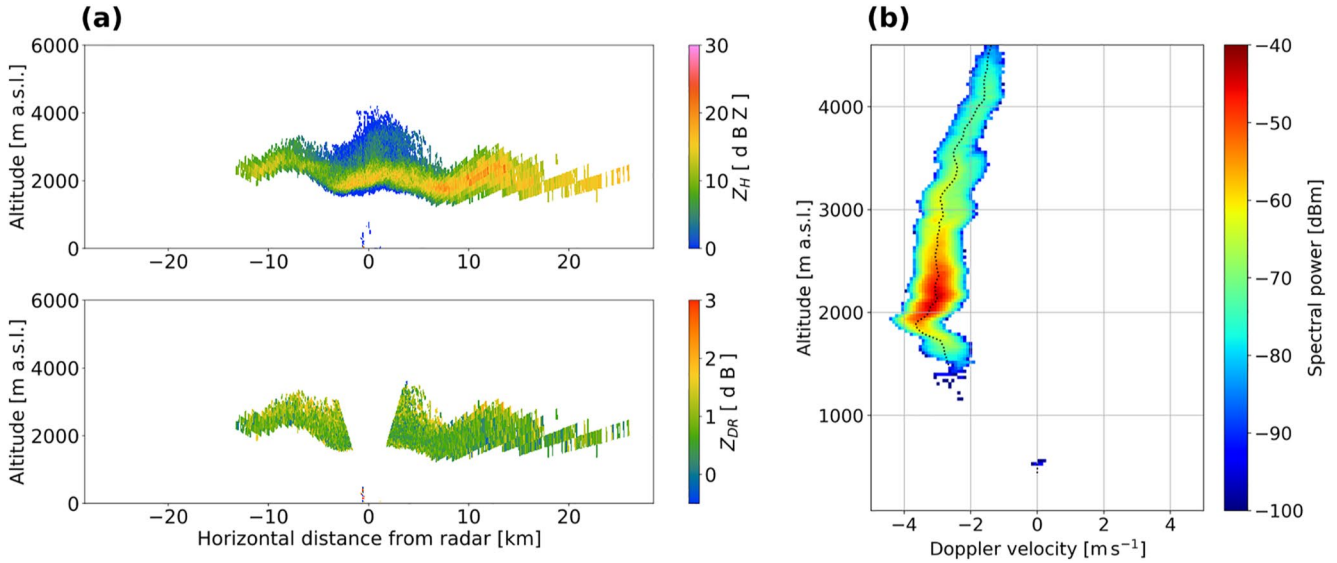

Figure 13. As for Figure 9 except at (a) 07:02 and (b) 07:00 UTC 10 January.

of temperature and relative humidity oscillations at the end of the event are due to the rapid successions of up- and downdrafts that brought the temperature up to 6 °C.

From about 20:00 UTC 09 January to 04:00 UTC 10 January a zone of intense aggregation is present (Figures 5c and 5d). The high values of D_{mean} simulated by WRF is once again qualitatively consistent with the high values of DFR, especially between 22:00 UTC 09 January and 00:00 UTC 10 January. The zone of dominating aggregates in MXPol classification corresponds well to the high values of DFR and shows also some rimed particles (red-magenta shading in Figure 5c). The lidar also detected SLW just above this mixture of aggregates and rimed particles. Note that the presence of hydrometeors further down in MXPol classification compared to BASTA is because all RHIs at an horizontal range greater than 6 km have been considered in MXPol classification, showing that the sublimation height has significant spatial heterogeneity. Unlike during Phase I, where the zone of aggregation was topped by a layer of intense depositional growth leading to high Z_{DR} values, during Phase III the layer of aggregation is topped by smaller Z_{DR} values (Figure 8) and aggregation is identified solely by the increase in Z_H and DFR.

On 10 January between 04:00 and 09:00 UTC, apparent nonstationary OGWs trapped in the low- and mid-troposphere can be seen as a succession of intense up- and downdrafts with Doppler velocities of more than 2 m s^{-1} and a periodicity of about an hour (Figure 5b). The apparent nonstationary nature of these OGWs likely owes to the decrease in wind speed upstream of the ridge (compare Figures 10a and 12a). WRF simulations revealed that the OGWs are propagating upstream (not shown). We hypothesize that this upstream propagation is a consequence of the gravity wave train adapting to the weaker forcing, which leads to the apparent nonstationary OGWs (Nance & Durran, 1997). These vertical motions strongly affect the vertical structure of the cloud as can be seen by the fluctuating level of maximum reflectivity (Figure 5a). This can also be seen in MXPol measurements (Figure 13), where the OGWs lead to an oscillation of the height of sublimation and to a shift of the whole Doppler spectrum. The mean Doppler velocity at cloud top is of about −2 m s^{-1} and its magnitude increases with decreasing height as the hydrometeors likely become denser and fall faster. The rapid change from about −3 to −4 m s^{-1} at 2,000 m is probably due to an increase in the magnitude of the downdraft. The horizontal wavelength of the OGWs is about 10 km and is consistent between MXPol measurements and WRF simulation (Figures 13b and 12b). The OGWs are also associated with rapid fluctuations of temperature and relative humidity (Figure 5f). These OGWs become visible (compared to earlier phases) in a time-series of vertical Doppler velocity above Davis because (a) they are nonstationary, (b) they are present far enough downstream of the ice plateau and (c) they are sufficiently strong to lift the hydrometeors and hence lead to positive vertical Doppler velocities. Note that these strong OGWs coincide with winds shifting to easterlies for the first time during the event around 3,000 m, showing again that their generation depends on the wind direction.

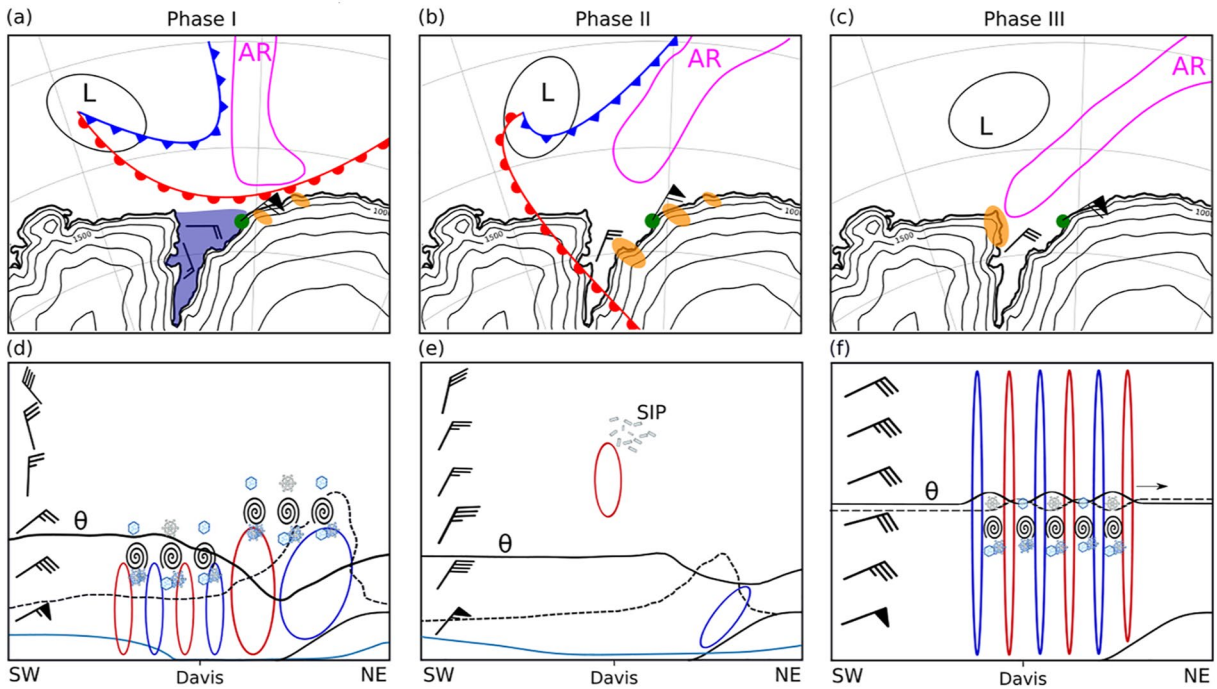

Figure 14. Conceptual model of the three phases of the event. (a)–(c) maps as in Figure 3. "L" represents the low pressure system, the blue area the cold air pool. The orange shapes represent precipitation maxima, the green dot Davis. (d)–(f) cross-sections as in Figure 7b. The blue and red shapes show downdrafts and updrafts, respectively. The black line in the bottom panels shows an isentrope, the dashed line the height of saturation w.r.t. ice, and the blue line the qualitative variation of precipitation rate along the cross-section. Only the main microphysical processes are represented.

In summary, Phase III is characterized by a north-easterly flow generating nonstationary OGWs, which are evident in vertical Doppler velocity measurements and lead to a fluctuation of the level of sublimation.

4.4. Summary of the Three Phases

Figure 14 shows a conceptual model of the three phases of the event. During Phase I, Davis is located just ahead of the warm front and the low-level flow is north-easterly. The cold front is directing the AR meridionally to the coast with precipitation maxima on the windward slopes ahead of the warm front (Figure 14a, orange shading). Due to the sharp horizontal temperature gradient between the cold air pool over Prydz Bay and the warm sector of the cyclone, the thermal wind is directed to the east and leads to backing winds with height. This thermal wind leads to a barrier wind over Prydz Bay, which protects the Amery Ice Shelf from the large-scale flow. The north-easterly flow provides favorable conditions, with respect to the orography, for the generation of trapped OGWs, which are excited at the temperature inversion at the top of the boundary layer (Hills et al., 2016). The turbulence at the top of the OGWs might enhance aggregation, which is visible in the hydrometeor classification (Figure 5c), the maxima of DFR (Figure 5d), and the polarimetric variables (Figure 8). Despite the advection of moisture by the AR and the intense aggregation, the foehn effect creates a tongue of relatively dry air that spreads over the Vestfold Hills leading to sublimation of snowfall below 1,000 m a.s.l., as can be seen in the reflectivity profiles (Figure 5a).

During Phase II, the surface cyclone has moved eastwards. Davis is in the warm sector, the cold air pool has been eroded, which allows the moisture advected by the AR to enter Prydz Bay, leading to precipitation maxima on the windward slopes of the Ingrid Christensen Coast. Another consequence after the passage of the warm front is the weaker horizontal temperature gradient over Davis, which reduces the thermal wind, such that the flow is north-northeasterly at all heights (Figure 14e). Since the flow is north-northeasterly, it does not impinge perpendicularly on the orography upstream of Davis, which reduces the foehn effect. As a result, the boundary layer is moister, the sublimation is less intense and snowfall does reach the ground at Davis. The absence of low-level OGWs coincides with the lack of intense aggregation, which leads to overall smaller reflectivity values than during Phase I. A layer of moderate updrafts ($\sim 1\,\mathrm{m\,s^{-1}}$) between about 3,000 m and 4,000 m could be identified in Doppler velocity measurements and the WRF simulation and is attributed to a gravity wave train located

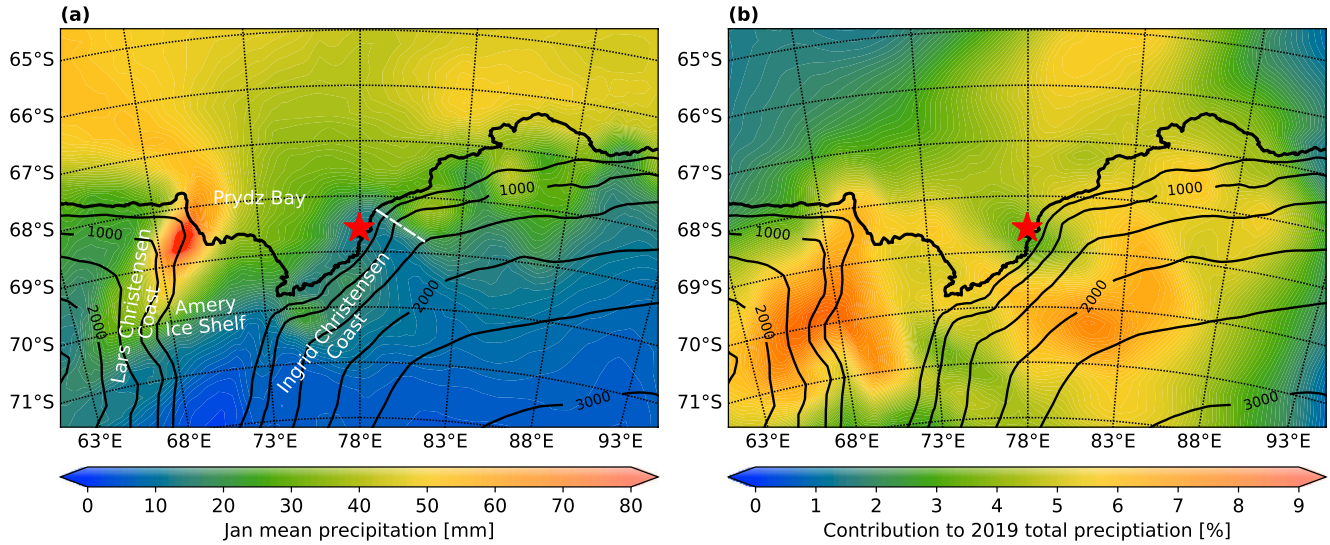

Figure 15. (a) Precipitation climatology for January computed from 1969 to 2020. Davis is marked with the red star. Geographical features and the axis of the ice ridgeline (white dashed line) are indicated in (a). (b) Ratio of the precipitation accumulated from 07 January 19 UTC to 10 January 19 UTC to the 2019 annual precipitation. All data are from the ERA5 reanalysis. The black contours show the ERA5 topography in m a.s.l. The thicker contour shows the coast and the ice-edge.

downstream of the ridge to the north-east of Davis. This moderate updraft is also associated with a bimodality in radar Doppler spectra, which is likely due to secondary ice production by collisional breakup of ice crystals.

During Phase III, the low pressure system has split in two, the fronts have moved eastward with one of them, while the other one is directing the AR to the north of the Lars Christensen Coast, leading to the largest precipitation accumulation over the whole event (Figure 2). The flow is oriented north-easterly at all heights providing the ideal conditions for the generation of OGWs. As opposed to the OGWs during Phase I, they are nonstationary and lead to a succession of strong up- and downdrafts with a period of about 1 h visible in Doppler velocity measurements (Figure 5b). The vertical gradient of relative humidity below 2,000 m is the largest of the event (Figure 6b) and lead to total sublimation within about 200 m of cloud base. Phase III marks the end of the event, before the PV cutoff and associated low pressure decays and a high-pressure ridge directs a dry flow to Prydz Bay (not shown).

5. Regional Climatological Perspective

A question that arises from the results of this case study is: how representative is it in the climatology? We consider this question in this section, by discussing the possible climatological implications of our results using ERA5 reanalysis. Figure 2 indicated that orography played a major role in the distribution of precipitation during this event. This is supported by the results shown in Section 4 and we showed that the direction of the large-scale flow with respect to the orography dictates the precipitation accumulation pattern. Given that north-easterly is the most frequent flow direction during precipitation events over Davis (Figure 4 of Vignon, Traullé, & Berne, 2019), one might suspect that the precipitation accumulation shown in Figure 2 could be climatologically representative. This is supported by the ERA5 climatology (Figure 15a), which shows a maximum on the Lars Christensen Coast, in particular in its northernmost part, while the Ingrid Christensen Coast is much dryer, especially the region around the Vestfold Hills. This distribution is remarkably similar to the one of this event (Figure 2), suggesting it is representative of the January climatology in terms of spatial distribution. Note that a comparison between precipitation accumulation from ERA5 with WRF 9-km resolution domain over the event showed that the spatial distribution is very similar, but that ERA5 exhibits a smaller spread between maxima and minima compared to WRF, mostly owing to the difference in resolution. For instance the maximum on the windward side of the ice ridgeline to the north-east of Davis (Figure 2) is smaller and the minimum over Davis is larger in ERA5 compared to WRF. Therefore, we restrict our comparison to the spatial distribution. The contribution of this event to the annual total precipitation of 2019 is up to 8% in the interior of the Lars Christensen Coast and around 2% in the Vestfold Hills (Figure 15b).

Figure 15 only allows us to compare the precipitation distribution of our case study with the climatology, but does not make it possible to ascertain the main synoptic configurations associated with intense precipitation over Prydz

Bay. Some recent studies however allow us to bring the large-scale features of our case study in a climatological perspective. Yu et al. (2018) studied the synoptic patterns associated with extreme precipitation at Progress station, which is located 110 km to the south-west of Davis on the Ingrid Christensen Coast. They found out that a dipole structure with a low (high) geopotential height anomaly to the north-west (north-east) of Prydz Bay together with a north-easterly advection of moisture is the dominant synoptic pattern associated with extreme precipitation at Progress station. They also mention that the ascending motions over Progress station provides favorable conditions for extreme precipitation. This synoptic description resembles the one presented in Section 3, suggesting that the synoptic conditions of our case study can be representative of extreme precipitation over Prydz Bay. Further recent studies showed that Prydz Bay is prone to intense precipitation events by enhanced meridional moisture advections. First, Turner et al. (2019) showed that 50% of the annual precipitation is received in less than 10 days of the heaviest precipitation over the Amery Ice Shelf. They attribute this to quasi-stationary depressions, which can occasionally transport moisture far into the Amery Ice Shelf in regions normally sheltered by the orography. The quasi-stationary nature of the PV cutoff described in Section 3 and the fact that it directs an increasingly more easterly flow (ideal for orographic enhancement on the the Lars Christensen Coast) explains the relatively high contribution to the 2019 annual precipitation on the Lars Christensen coast (Figure 15b). Second, Portmann et al. (2021) showed that Prydz Bay is located poleward of the band of high frequency of PV cutoffs around Antarctica (their Figure 3). Furthermore, Ch. 3 of Portmann (2020) investigated the relevance of PV cutoffs for precipitation. They found that cutoffs involving enhanced meridional moisture transport contribute the most to extreme precipitation events. Since, our case both features a PV cutoff to the north of Prydz Bay and intense meridional moisture transport, it suggests that similar synoptic configurations are common and do contribute to extreme precipitation over Prydz Bay. Wille et al. (2021) studied the precipitation impact of ARs in Antarctica. They showed that the frequency of ARs above Prydz Bay was about 2 days per year. They also investigated the attribution of extreme precipitation events to ARs. Their Figure 4c shows a strong dipole over the Ingrid Christensen Coast, with the Vestfold Hills being located in a region with less than 10% of EPEs attributed to ARs, while further north-east on the coast up to 50% of EPEs are attributed to ARs. This suggests that the contribution of ARs to EPEs over Prydz Bay is highly variable, consistent with Figures 2 and 15b. We showed that local processes can be determinant in how much an AR event contribute to the annual precipitation accumulation. Furthermore, Figure 3b of Wille et al. (2021) shows large AR-related snowfall on the eastern sides of ice ridgelines, including the one to the north-east of Davis. The Vestfold Hills also appear as a minimum of total AR-related snowfall. This suggests that our case study is representative of large snowfall accumulation from ARs around East Antarctica. Finally, it also confirms our finding that local processes related to the orography, such as a foehn wind, can determine the fate of large-scale moisture advections from ARs. The study of Grazioli et al. (2017) shows that the Vestfold Hills are in a region of maximum ratio of sublimated snowfall with up to 48% of total snowfall sublimating before reaching the ground. They attribute low-level sublimation to dry katabatic winds, but they also mention that foehn winds can play an important role in the Antarctic Peninsula. Our study shows that foehn winds can lead to total snowfall sublimation also in East Antarctica and be as efficient as katabatics in doing so, at least at the scale of one event. While, the foehn effect is a local process, the dynamical triggering comes more often from the large-scale flow. As stated by Bozkurt et al. (2018), it is hence difficult to totally disentangle the role of local versus large-scale processes during foehn events. In the end the interactions between the synoptic flow, the orography, and the regional-scale circulation determine the impact on precipitation.

Overall, the ERA5 climatology shown in Figure 15 and the studies of Portmann et al. (2021), Turner et al. (2019), and Wille et al. (2021) show that we can expect the synoptic configuration of our case study to be representative of EPEs over Prydz Bay, at least in austral summer. In this view, we can hypothesize that the processes at play for snowfall sublimation over Davis shown in Section 4 might substantially contribute to the precipitation climatology of the Vestfold Hills.

6. Conclusions

In this study, we analyzed the precipitation distribution and microphysics associated with an intense meridional moisture transport affected by OGWs over Prydz Bay, Antarctica. The complementary nature of remote-sensing instruments and WRF simulation allowed us to link local observations with the complex dynamics of this event. We divided the event into three distinct phases. Our findings can be summarized as follows:

1. The direction of the synoptic flow was the dominant factor driving the occurrence of OGWs over Davis, with an easterly to north-easterly flow favoring the development of low-level OGWs, while a north-northeasterly

flow inhibited such low-level OGWs. The presence of a statically stable layer favored the trapping of the OGWs below 2,000 m during Phase I

2. A foehn effect produced a dry air flow that spread over the Vestfold Hills and led to total snowfall sublimation during Phase I and Phase III. During Phase II, the wind backed to north-northeasterly inhibiting the formation of low-level OGWs above Davis and hence reducing the dryness of the boundary layer, which led to light snowfall reaching the ground
3. The turbulence generated at the top of the trapped OGWs during Phase I might have led to intense aggregation, which was observable in dual-polarization and dual-frequency radar variables. During Phase II, a persistent updraft associated with a mid-level stationary gravity wave train was visible in the radar Doppler velocity. Analyses of the Doppler spectrograms showed that this updraft was associated with a bimodality, which we attributed to the production of secondary ice by collisional breakup of ice particles. During Phase III, nonstationary OGWs can be clearly seen in vertical Doppler velocity measurements and lead to a fluctuation of the level of maximum reflectivity. Those OGWs are qualitatively well represented by WRF, although the magnitude is underestimated and the phase shifted

This study showed that despite the intense meridional moisture advection by an AR, local processes tied to the orography determined the spatial and temporal distribution of precipitation over Prydz Bay. This stresses the importance of studying local effects when interpreting the impact of ARs in terms of surface precipitation at the regional scale. Moreover, it suggests that climate models projections and satellite measurements over regions where local processes dictate the precipitation patterns should be interpreted with care. Similarly to the study of Grazioli et al. (2017), we showed that the fate of precipitation in Antarctica often comes down to complex interactions between the large-scale flow, the orography, and regional circulations, such as foehn and katabatic winds. Future studies should concentrate on the synoptic configurations during precipitation and sublimation events over Prydz Bay to determine whether the mechanisms proposed here can explain the rather peculiar precipitation climatology of Prydz Bay, and in particular of the Vestfold Hills.

Appendix A: Satellite Image

Figure A1 shows an infrared satellite image on 10 January 2019. The cloud structure associated with the OGWs is clearly visible downstream of the ice ridgeline that is located to the north-east of Davis. These orographic clouds extend as far as about 150 km downstream over the Amery Ice Shelf.

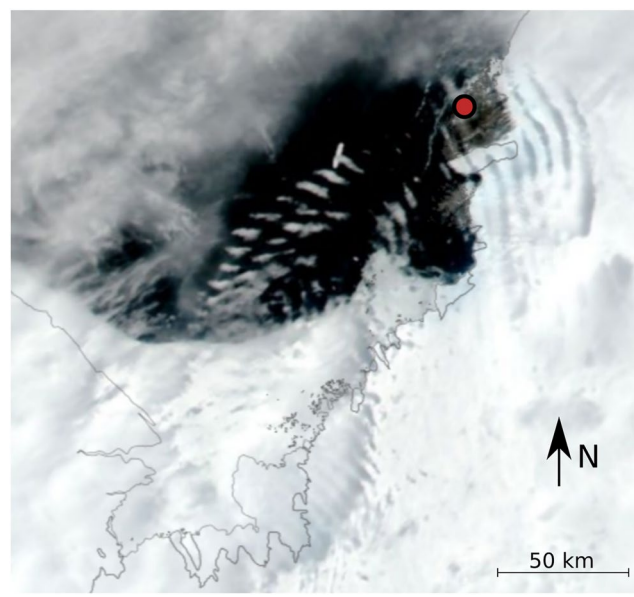

Figure A1. Corrected reflectance (true color) of the Suomi National Polar orbiting Partnership/Visible Infrared Imaging Radiometer Suite satellite overpass of 10 January 2019. The imagery resolution is 250 m. The red dot shows the location of Davis station.

Data Availability Statement

All observations and simulation data are available on https://doi.org/10.1594/PANGAEA.939340. The VHF radar data are also available on https://data.aad.gov.au/metadata/records/Davis_MST_Radar.

Acknowledgments
The authors thank J. Grazioli for his insightful comments on our study. The authors thank J.D. Wille for checking that our event qualifies as an AR. J. Gehring and A. Ferrone received financial support from the Swiss National Science Foundation (grant no. 175700/1). É. Vignon received financial support from the EPFL-LOSUMEA project. The contribution of A. Protat to this project was supported by the National Environmental Science Program (NESP) and the Australian Antarctic Partnership Program (AAPP). Deployment of the instrumentation to Davis, and the contribution of S.P. Alexander to this project, was supported by the Australian Antarctic Division through Australian Antarctic Science Projects 4292 and 4387. The VHF radar is supported by Australian Antarctic Science Project 4445. The authors thank Ken Barrett, Chris Young, Derryn Harvie, Mike Hyde, Andrew Klekociuk and Angus Davis for their assistance in preparation, installation and commissioning of the instruments at Davis.

References

Agosta, C., Amory, C., Kittel, C., Orsi, A., Favier, V., Gallée, H., et al. (2019). Estimation of the Antarctic surface mass balance using the regional climate model MAR (1979–2015) and identification of dominant processes. *The Cryosphere*, *13*(1), 281–296. https://doi.org/10.5194/tc-13-281-2019

Alexander, S. P., McFarquhar, G. M., Marchand, R., Protat, A., Vignon, E., Mace, G. G., & Klekociuk, A. R. (2021). Mixed-phase clouds and precipitation in Southern Ocean cyclones and cloud systems observed poleward of 64°S by ship-based cloud radar and lidar. *Journal of Geophysical Research: Atmospheres*, *126*(8), e2020JD033626. https://doi.org/10.1029/2020JD033626

Alexander, S. P., & Murphy, D. (2015). The seasonal cycle of lower-tropospheric gravity wave activity at Davis, Antarctica (69°S, 78°E). *Journal of the Atmospheric Sciences*, *72*(3), 1010–1021. https://doi.org/10.1175/JAS-D-14-0171.1

Alexander, S. P., Orr, A., Webster, S., & Murphy, D. J. (2017). Observations and fine-scale model simulations of gravity waves over Davis, East Antarctica (69°S, 78°E). *Journal of Geophysical Research: Atmospheres*, *122*(14), 7355–7370. https://doi.org/10.1002/2017JD026615

Alexander, S. P., & Protat, A. (2018). Cloud properties observed from the surface and by satellite at the northern edge of the Southern Ocean. *Journal of Geophysical Research: Atmospheres*, *123*(1), 443–456. https://doi.org/10.1002/2017JD026552

Alexander, S. P., & Protat, A. (2019). Vertical profiling of aerosols with a combined Raman-elastic backscatter lidar in the remote Southern Ocean marine boundary layer (43–66°S, 132–150°E). *Journal of Geophysical Research: Atmospheres*, *124*(22), 12107–12125. https://doi.org/10.1029/2019JD030628

Atlas, D., & Ludlam, F. H. (1961). Multi-wavelength radar reflectivity of hailstorms. *Quarterly Journal of the Royal Meteorological Society*, *87*(374), 523–534. https://doi.org/10.1002/qj.49708737407

Bailey, M. P., & Hallett, J. (2009). A comprehensive habit diagram for atmospheric ice crystals: Confirmation from the laboratory, AIRS II, and other field studies. *Journal of the Atmospheric Sciences*, *66*(9), 2888–2899. https://doi.org/10.1175/2009JAS2883.1

Battaglia, A., Tanelli, S., Tridon, F., Kneifel, S., Leinonen, J., & Kollias, P. (2020). Triple-frequency radar retrievals. In V. Levizzani, C. Kidd, D. B. Kirschbaum, C. D. Kummerow, K. Nakamura, & F. J. Turk (Eds.), *Satellite precipitation measurement* (Vol. 1, pp. 211–229). Springer International Publishing. https://doi.org/10.1007/978-3-030-24568-9_13

Besic, N., Gehring, J., Praz, C., Figueras i Ventura, J., Grazioli, J., Gabella, M., et al. (2018). Unraveling hydrometeor mixtures in polarimetric radar measurements. *Atmospheric Measurement Techniques*, *11*(8), 4847–4866. https://doi.org/10.5194/amt-11-4847-2018

Bozkurt, D., Rondanelli, R., Marín, J. C., & Garreaud, R. (2018). Foehn event triggered by an Atmospheric River underlies record-setting temperature along continental Antarctica. *Journal of Geophysical Research: Atmospheres*, *123*(8), 3871–3892. https://doi.org/10.1002/2017JD027796

Cape, M. R., Vernet, M., Skvarca, P., Marinsek, S., Scambos, T., & Domack, E. (2015). Foehn winds link climate-driven warming to ice shelf evolution in Antarctica. *Journal of Geophysical Research: Atmospheres*, *120*(21), 11037–11057. https://doi.org/10.1002/2015JD023465

Carbone, R. E., Atlas, D., Eccles, P., Fetter, R., & Mueller, E. (1973). Dual wavelength radar hail detection. *Bulletin of the American Meteorological Society*, *54*(9), 9212–924. https://doi.org/10.1175/1520-0477(1973)054<0921:dwrhd>2.0.co;2

Connolly, P. J., Emersic, C., & Field, P. R. (2012). A laboratory investigation into the aggregation efficiency of small ice crystals. *Atmospheric Chemistry and Physics*, *12*(4), 2055–2076. https://doi.org/10.5194/acp-12-2055-2012

Damiens, F., Lott, F., Millet, C., & Plougonven, R. (2018). An adiabatic foehn mechanism. *Quarterly Journal of the Royal Meteorological Society*, *144*(714), 1369–1381. https://doi.org/10.1002/qj.3272

Delanoë, J., Protat, A., Vinson, J.-P., Brett, W., Caudoux, C., Bertrand, F., et al. (2016). BASTA: A 95-GHz FMCW Doppler radar for cloud and Fog studies. *Journal of Atmospheric and Oceanic Technology*, *33*(5), 1023–1038. https://doi.org/10.1175/JTECH-D-15-0104.1

Eccles, P. J., & Atlas, D. (1973). A dual-wavelength radar hail detector. *Journal of Applied Meteorology and Climatology*, *12*(5), 8472–854. https://doi.org/10.1175/1520-0450(1973)012<0847:adwrhd>2.0.co;2

Elvidge, A. D., Renfrew, I. A., King, J. C., Orr, A., & Lachlan-Cope, T. A. (2016). Foehn warming distributions in nonlinear and linear flow regimes: A focus on the Antarctic Peninsula. *Quarterly Journal of the Royal Meteorological Society*, *142*(695), 618–631. https://doi.org/10.1002/qj.2489

Elvidge, A. D., Renfrew, I. A., King, J. C., Orr, A., Lachlan-Cope, T. A., Weeks, M., & Gray, S. L. (2015). Foehn jets over the Larsen C ice shelf, Antarctica. *Quarterly Journal of the Royal Meteorological Society*, *141*(688), 698–713. https://doi.org/10.1002/qj.2382

Ferrone, A., & Berne, A. (2021). Dynamic differential reflectivity calibration using vertical profiles in rain and snow. *Remote Sensing*, *13*(1), 8. https://doi.org/10.3390/rs13010008

Gehring, J., Ferrone, A., Billault-Roux, A.-C., Besic, N., Ahn, K. D., Lee, G., & Berne, A. (2021). Radar and ground-level measurements of precipitation collected by the École Polytechnique Fédérale de Lausanne during the International collaborative experiments for PyeongChang 2018 olympic and paralympic winter games. *Earth System Science Data*, *13*(2), 417–433. https://doi.org/10.5194/essd-13-417-2021

Gerber, F., & Lehning, M. (2020). *REMA topography and AntarcticaLC2000 for WRF*. EnviDat. https://doi.org/10.16904/envidat.190

Gorodetskaya, I. V., Tsukernik, M., Claes, K., Ralph, M. F., Neff, W. D., & Lipzig, N. P. M. V. (2014). The role of atmospheric rivers in anomalous snow accumulation in East Antarctica. *Geophysical Research Letters*, *41*(17), 6199–6206. https://doi.org/10.1002/2014GL060881

Grazioli, J., Madeleine, J.-B., Gallée, H., Forbes, R. M., Genthon, C., Krinner, G., & Berne, A. (2017). Katabatic winds diminish precipitation contribution to the Antarctic ice mass balance. *Proceedings of the National Academy of Sciences*, *114*(41), 10858–10863. https://doi.org/10.1073/pnas.1707633114

Grosvenor, D. P., King, J. C., Choularton, T. W., & Lachlan-Cope, T. (2014). Downslope föhn winds over the Antarctic Peninsula and their effect on the Larsen ice shelves. *Atmospheric Chemistry and Physics*, *14*(18), 9481–9509. https://doi.org/10.5194/acp-14-9481-2014

Hallett, J., & Mossop, S. C. (1974). Production of secondary ice particles during the riming process. *Nature*, *249*(5452), 26–28. https://doi.org/10.1038/249026a0

Hersbach, H., Bell, B., Berrisford, P., Hirahara, S., Horányi, A., Muñoz-Sabater, J., et al. (2020). The ERA5 global reanalysis. *Quarterly Journal of the Royal Meteorological Society*, *146*(730), 1999–2049. https://doi.org/10.1002/qj.3803

Hills, M. O. G., Durran, D. R., & Blossey, P. N. (2016). The dissipation of trapped lee waves. Part II: The relative importance of the boundary layer and the stratosphere. *Journal of the Atmospheric Sciences*, *73*(3), 943–955. https://doi.org/10.1175/JAS-D-15-0175.1

Hines, K. M., & Bromwich, D. H. (2008). Development and testing of polar weather Research and Forecasting (WRF) model. Part I: Greenland ice sheet Meteorology. *Monthly Weather Review*, *136*(6), 1971–1989. https://doi.org/10.1175/2007MWR2112.1

Hobbs, P. V., Chang, S., & Locatelli, J. D. (1974). The dimensions and aggregation of ice crystals in natural clouds. *Journal of Geophysical Research*, *79*(15), 2199–2206. https://doi.org/10.1029/JC079i015p02199

Howat, I. M., Porter, C., Smith, B. E., Noh, M.-J., & Morin, P. (2019). The reference elevation model of Antarctica. *The Cryosphere*, *13*(2), 665–674. https://doi.org/10.5194/tc-13-665-2019

Iacono, M. J., Delamere, J. S., Mlawer, E. J., Shephard, M. W., Clough, S. A., & Collins, W. D. (2008). Radiative forcing by long-lived greenhouse gases: Calculations with the AER radiative transfer models. *Journal of Geophysical Research*, *113*(D13), D13103. https://doi.org/10.1029/2008JD009944

Janjić, Z. I. (1994). The step-mountain Eta coordinate model: Further developments of the convection, viscous sublayer, and turbulence closure schemes. *Monthly Weather Review*, *122*(5), 9272–945. https://doi.org/10.1175/1520-0493(1994)122<0927:TSMECM>2.0.CO;2

Kain, J. S., & Fritsch, J. M. (1990). A one-dimensional entraining/detraining plume model and its application in convective parameterization. *Journal of the Atmospheric Sciences*, *47*(23), 27842–2802. https://doi.org/10.1175/1520-0469(1990)047<2784:AODEPM>2.0.co;2

King, J. C., & Turner, J. (1997). *Antarctic meteorology and climatology*. Cambridge University Press.

Kirchgaessner, A., King, J. C., & Anderson, P. S. (2021). The impact of föhn conditions across the Antarctic Peninsula on local Meteorology based on AWS measurements. *Journal of Geophysical Research: Atmospheres*, *126*(4), e2020JD033748. https://doi.org/10.1029/2020JD033748

Klepp, C., Michel, S., Protat, A., Burdanowitz, J., Albern, N., Kähnert, M., et al. (2018). OceanRAIN, a new in-situ shipboard global ocean surface-reference dataset of all water cycle components. *Scientific Data*, *5*(1), 180122. https://doi.org/10.1038/sdata.2018.122

Klugmann, D., Heinsohn, K., & Kirtzel, H.-J. (1996). A low cost 24 GHz FM-CW Doppler radar rain profiler. *Contributions to Atmospheric Physics*, *69*(1), 247–253.

Kneifel, S., von Lerber, A., Tiira, J., Moisseev, D., Kollias, P., & Leinonen, J. (2015). Observed relations between snowfall microphysics and triple-frequency radar measurements. *Journal of Geophysical Research: Atmospheres*, *120*, 6034–6055. https://doi.org/10.1002/2015JD023156

Korolev, A., & Leisner, T. (2020). Review of experimental studies of secondary ice production. *Atmospheric Chemistry and Physics*, *20*(20), 11767–11797. https://doi.org/10.5194/acp-20-11767-2020

Libbrecht, K. G. (2005). The physics of snow crystals. *Reports on Progress in Physics*, *68*(4), 855–895. https://doi.org/10.1088/0034-4885/68/4/R03

Mace, G. G., & Protat, A. (2018). Clouds over the Southern Ocean as observed from the R/V investigator during CAPRICORN. Part I: Cloud occurrence and phase partitioning. *Journal of Applied Meteorology and Climatology*, *57*(8), 1783–1803. https://doi.org/10.1175/JAMC-D-17-0194.1

Matrosov, S. Y. (1998). A dual-wavelength radar method to measure snowfall rate. *Journal of Applied Meteorology and Climatology*, *37*(11), 15102–1521. https://doi.org/10.1175/1520-0450(1998)037<1510:adwrmt>2.0.co;2

McFarquhar, G. M., Bretherton, C. S., Marchand, R., Protat, A., DeMott, P. J., Alexander, S. P., et al. (2021). Observations of clouds, aerosols, precipitation, and surface radiation over the Southern Ocean: An overview of CAPRICORN, MARCUS, MICRE, and SOCRATES. *Bulletin of the American Meteorological Society*, *102*(4), E894–E928. https://doi.org/10.1175/BAMS-D-20-0132.1

Moffat-Griffin, T. (2019). An introduction to atmospheric gravity wave science in the polar regions and first results from ANGWIN. *Journal of Geophysical Research: Atmospheres*, *124*(3), 1198–1199. https://doi.org/10.1029/2019JD030247

Morrison, H., Curry, J. A., & Khvorostyanov, V. I. (2005). A new double-moment microphysics parameterization for application in cloud and climate models. Part I: Description. *Journal of the Atmospheric Sciences*, *62*(6), 1665–1677. https://doi.org/10.1175/JAS3446.1

Nance, L. B., & Durran, D. R. (1997). A modeling study of nonstationary trapped mountain lee waves. Part I: Mean-flow variability. *Journal of the Atmospheric Sciences*, *54*(18), 2275–2291. https://doi.org/10.1175/1520-0469(1997)054<2275:amsont>2.0.co;2

Niu, G.-Y., Yang, Z.-L., Mitchell, K. E., Chen, F., Ek, M. B., Barlage, M., et al. (2011). The community Noah land surface model with multiparameterization options (Noah-MP): 1. Model description and evaluation with local-scale measurements. *Journal of Geophysical Research*, *116*(D12), D12109. https://doi.org/10.1029/2010JD015139

Noh, Y.-J., Miller, S. D., Heidinger, A. K., Mace, G. G., Protat, A., & Alexander, S. P. (2019). Satellite-based detection of daytime supercooled liquid-topped mixed-phase clouds over the Southern Ocean using the advanced Himawari imager. *Journal of Geophysical Research: Atmospheres*, *124*(5), 2677–2701. https://doi.org/10.1029/2018JD029524

Noone, D., Turner, J., & Mulvaney, R. (1999). Atmospheric signals and characteristics of accumulation in dronning Maud land, Antarctica. *Journal of Geophysical Research*, *104*(D16), 19191–19211. https://doi.org/10.1029/1999JD900376

Nuncio, M., & Satheesan, K. (2014). Indian Ocean Dipole and southern high latitude precipitation: Possible links. *Climate Dynamics*, *43*(7–8), 1965–1972. https://doi.org/10.1007/s00382-013-2020-5

Orr, A., Phillips, T., Webster, S., Elvidge, A., Weeks, M., Hosking, S., & Turner, J. (2014). Met Office Unified Model high-resolution simulations of a strong wind event in Antarctica. *Quarterly Journal of the Royal Meteorological Society*, *140*(684), 2287–2297. https://doi.org/10.1002/qj.2296

Phillips, V. T. J., Formenton, M., Bansemer, A., Kudzotsa, I., & Lienert, B. (2015). A parameterization of sticking efficiency for collisions of snow and graupel with ice crystals: Theory and comparison with observations. *Journal of the Atmospheric Sciences*, *72*(12), 4885–4902. https://doi.org/10.1175/JAS-D-14-0096.1

Pickard, J. (1986). *Antarctic oases, Davis station and the Vestfold Hills* (pp. 1–19). Academic Press, Macquarie University.

Portmann, R. (2020). *The life cycles of potential vorticity cutoffs: Climatology, predictability, and high impact weather. Doctoral Thesis*, ETH Zurich. https://doi.org/10.3929/ethz-b-000466735

Portmann, R., Sprenger, M., & Wernli, H. (2021). The three-dimensional life cycles of potential vorticity cutoffs: A global and selected regional climatologies in ERA-Interim (1979–2018). *Weather and Climate Dynamics*, *2*(2), 507–534. https://doi.org/10.5194/wcd-2-507-2021

Protat, A., Klepp, C., Louf, V., Petersen, W. A., Alexander, S. P., Barros, A., et al. (2019). The latitudinal variability of oceanic rainfall properties and its implication for satellite retrievals: 1. Drop size distribution properties. *Journal of Geophysical Research: Atmospheres*, *124*(23), 13291–13311. https://doi.org/10.1029/2019JD031010

Ralph, F. M., Neiman, P. J., & Wick, G. A. (2004). Satellite and CALJET aircraft observations of atmospheric rivers over the eastern north Pacific ocean during the winter of 1997/98. *Monthly Weather Review*, *132*(7), 1721–1745. https://doi.org/10.1175/1520-0493(2004)132<1721:sacaoo>2.0.co;2

Ralph, F. M., Neiman, P. J., Wick, G. A., Gutman, S. I., Dettinger, M. D., Cayan, D. R., & White, A. B. (2006). Flooding on California's Russian River: Role of atmospheric rivers. *Geophysical Research Letters*, *33*(13). https://doi.org/10.1029/2006GL026689

Royer, P., Bizard, A., Sauvage, L., & Thobois, L. (2014). Validation protocol and intercomparison campaigns with the R-MAN510 aerosol lidar. In *Proc. 17th International Symposium for the advancement of boundary-layer remote sensing*.

Sachsperger, J., Serafin, S., Grubišić, V., Stiperski, I., & Paci, A. (2017). The amplitude of lee waves on the boundary-layer inversion. *Quarterly Journal of the Royal Meteorological Society*, *143*(702), 27–36. https://doi.org/10.1002/qj.2915

Schneebeli, M., Dawes, N., Lehning, M., & Berne, A. (2013). High-resolution vertical profiles of X-band polarimetric radar observables during snowfall in the Swiss Alps. *Journal of Applied Meteorology and Climatology*, *52*(2), 378–394. https://doi.org/10.1175/JAMC-D-12-015.1

Schrom, R. S., & Kumjian, M. R. (2016). Connecting microphysical processes in Colorado winter storms with vertical profiles of radar observations. *Journal of Applied Meteorology and Climatology*, *55*(8), 1771–1787. https://doi.org/10.1175/JAMC-D-15-0338.1

Shepherd, A., & Wingham, D. (2007). Recent sea-level contributions of the Antarctic and Greenland ice sheets. *Science*, *315*(5818), 1529–1532. https://doi.org/10.1126/science.1136776

Sotiropoulou, G., Vignon, E., Young, G., Morrison, H., O'Shea, S. J., Lachlan-Cope, T., et al. (2021). Secondary ice production in summer clouds over the Antarctic coast: An underappreciated process in atmospheric models. *Atmospheric Chemistry and Physics*, *21*(2), 755–771. https://doi.org/10.5194/acp-21-755-2021

Speirs, J. C., Steinhoff, D. F., McGowan, H. A., Bromwich, D. H., & Monaghan, A. J. (2010). Foehn winds in the McMurdo dry Valleys, Antarctica: The origin of extreme warming events. *Journal of Climate*, *23*(13), 3577–3598. https://doi.org/10.1175/2010JCLI3382.1

Steinhoff, D. F., Bromwich, D. H., & Monaghan, A. (2013). Dynamics of the foehn mechanism in the McMurdo dry Valleys of Antarctica from polar WRF. *Quarterly Journal of the Royal Meteorological Society*, *139*(675), 1615–1631. https://doi.org/10.1002/qj.2038

Summerson, R., & Bishop, I. D. (2011). Aesthetic value in Antarctica: Beautiful or sublime? *The Polar Journal*, *1*(2), 225–250. https://doi.org/10.1080/2154896X.2011.626626

Takahashi, T., Nagao, Y., & Kushiyama, Y. (1995). Possible high ice particle production during graupel–graupel collisions. *Journal of the Atmospheric Sciences*, *52*(24), 4523–4527. https://doi.org/10.1175/1520-0469(1995)052<4523:phippd>2.0.co;2

Tridon, F., Battaglia, A., Chase, R. J., Turk, F. J., Leinonen, J., Kneifel, S., et al. (2019). The microphysics of stratiform precipitation during OLYMPEX: Compatibility between triple-frequency radar and airborne in situ observations. *Journal of Geophysical Research: Atmospheres*, *124*(15), 8764–8792. https://doi.org/10.1029/2018JD029858

Turner, J., Phillips, T., Thamban, M., Rahaman, W., Marshall, G. J., Wille, J. D., et al. (2019). The dominant role of extreme precipitation events in Antarctic snowfall variability. *Geophysical Research Letters*, *46*, 3502–3511. https://doi.org/10.1029/2018GL081517

Valkonen, T., Vihma, T., Kirkwood, S., & Johansson, M. M. (2010). Fine-scale model simulation of gravity waves generated by Basen nunatak in Antarctica. *Tellus A: Dynamic Meteorology and Oceanography*, *62*(3), 319–332. https://www.tandfonline.com/doi/abs/10.1111/j.1600-0870.2009.00443.x

van den Broeke, M. R., & Gallée, H. (1996). Observation and simulation of barrier winds at the western margin of the Greenland ice sheet. *Quarterly Journal of the Royal Meteorological Society*, *122*(534), 1365–1383. https://doi.org/10.1002/qj.49712253407

Vardiman, L. (1978). The generation of secondary ice particles in clouds by crystal–crystal collision. *Journal of the Atmospheric Sciences*, *35*(11), 2168–2180. https://doi.org/10.1175/1520-0469(1978)035<2168:tgosip>2.0.co;2

Vignon, E., Alexander, S. P., DeMott, P. J., Sotiropoulou, G., Gerber, F., Hill, T. C. J., et al. (2021). Challenging and improving the simulation of mid-level mixed-phase clouds over the high-latitude Southern Ocean. *Journal of Geophysical Research: Atmospheres*, *126*, e2020JD033490. https://doi.org/10.1029/2020JD033490

Vignon, E., Besic, N., Jullien, N., Gehring, J., & Berne, A. (2019a). Microphysics of snowfall over coastal east Antarctica simulated by polar WRF and observed by radar. *Journal of Geophysical Research: Atmospheres*, *124*(21), 11452–11476. https://doi.org/10.1029/2019JD031028

Vignon, E., Picard, G., Durán Alarcón, C., Alexander, S. P., Gallée, H., & Berne, A. (2020). Gravity wave excitation during the coastal transition of an extreme katabatic flow in Antarctica. *Journal of the Atmospheric Sciences*, *77*, 1295–1312. https://doi.org/10.1175/JAS-D-19-0264.1

Vignon, E., Traullé, O., & Berne, A. (2019). On the fine vertical structure of the low troposphere over the coastal margins of East Antarctica. *Atmospheric Chemistry and Physics*, *19*(7), 4659–4683. https://doi.org/10.5194/acp-19-4659-2019

Vosper, S. B., Ross, A. N., Renfrew, I. A., Sheridan, P., Elvidge, A. D., & Grubišić, V. (2018). Current challenges in orographic flow dynamics: Turbulent exchange due to low-level gravity-wave processes. *Atmosphere*, *9*(9), 361. https://doi.org/10.3390/atmos9090361

Watanabe, S., Sato, K., & Takahashi, M. (2006). A general circulation model study of the orographic gravity waves over Antarctica excited by katabatic winds. *Journal of Geophysical Research*, *111*(D18), D18104. https://doi.org/10.1029/2005JD006851

Welker, C., Martius, O., Froidevaux, P., Reijmer, C. H., & Fischer, H. (2014). A climatological analysis of high-precipitation events in Dronning Maud Land, Antarctica, and associated large-scale atmospheric conditions: High precipitation in Dronning Maud Land. *Journal of Geophysical Research: Atmospheres*, *119*(21), 11932–11954. https://doi.org/10.1002/2014JD022259

Wille, J. D., Favier, V., Gorodetskaya, I. V., Agosta, C., Kittel, C., Beeman, J. C., et al. (2021). Antarctic atmospheric river climatology and precipitation impacts. *Journal of Geophysical Research: Atmospheres*, *126*(8), e2020JD033788. https://doi.org/10.1029/2020JD033788

Young, G., Lachlan-Cope, T., O'Shea, S. J., Dearden, C., Listowski, C., Bower, K. N., et al. (2019). Radiative effects of secondary ice enhancement in coastal Antarctic clouds. *Geophysical Research Letters*, *46*(4), 2312–2321. https://doi.org/10.1029/2018GL080551

Yu, L., Yang, Q., Vihma, T., Jagovkina, S., Liu, J., Sun, Q., & Li, Y. (2018). Features of extreme precipitation at progress station, Antarctica. *Journal of Climate*, *31*(22), 9087–9105. https://doi.org/10.1175/JCLI-D-18-0128.1

Zhu, Y., & Newell, R. E. (1998). A proposed algorithm for moisture fluxes from atmospheric rivers. *Monthly Weather Review*, *126*(3), 7252–735. https://doi.org/10.1175/1520-0493(1998)126<0725:apafmf>2.0.co;2

Zou, X., Bromwich, D. H., Nicolas, J. P., Montenegro, A., & Wang, S.-H. (2019). West Antarctic surface melt event of January 2016 facilitated by föhn warming. *Quarterly Journal of the Royal Meteorological Society*, *145*(719), 687–704. https://doi.org/10.1002/qj.3460